Promoting core/surface homogeneity during flash sintering of 3YSZ ceramic by current path management: experimental and modelling studies

Yinsheng Li[a,b,*], Riccardo Torchio[c,*], Simone Falco[d,*], Piergiorgio Alotto[c], Zhengren Huang[b], Richard I. Todd[a]

[a]Department of Materials, University of Oxford, Parks Road, Oxford OX1 3PH, UK

[b]Engineering Laboratory of Advanced Energy Materials, Ningbo Institute of Materials Technology and Engineering, Chinese Academy of Sciences, 1219 Zhongguan West Road, Ningbo 315201, Zhejiang, China

[c]Department of Industrial Engineering, University of Padua, 35135 Padua, Italy

[d]Department of Engineering Science, University of Oxford, Parks Road, Oxford OX1 3PJ, UK

Corresponding authors:

derek.ys.li@hotmail.com (Y. Li), riccardo.torchio@unipd.it (R. Torchio), simone.falco@eng.ox.ac.uk (S. Falco)

Tel: +44 1865 273787

Fax: +44 1865 273783

Abstract

During flash sintering (FS) of ceramics, the heat loss by surface radiation is the main cause of temperature gradient between core and surface, which induces inhomogeneity in microstructure. To solve this problem, the judicious designing of sample geometry and electrodes configuration is proposed. Experimental and simulation results show that the application of dogbone shape, forked electrodes, and lower cross-section aspect ratio effectively shifts the current path in 3YSZ samples from core to near-surface during FS, compared to bar-shape samples with a single electrode at each end. Consequently, the temperature distribution becomes more uniform throughout the 3YSZ sample, resulting in increase in relative density from 92.7% to 99.7% and improved core/surface homogeneity in microstructure. These optimizations enable 3YSZ ceramics to obtain significant increase in flexural strength from 1203±17 MPa to 1501±15 MPa. A multiphysics model is implemented and compared with experimental results, which reveals the underlying mechanisms of improved sample homogeneity.

Keywords: Flash sintering; 3YSZ; Thermal gradient; Multiphysics modelling; Microstructure

1. Introduction

Flash sintering (FS) is a new type of electric field assisted sintering method first reported by Cologna et al. in 2010 [1]. In this method, ceramics can be sintered in just a few seconds by the application of a sufficiently high electric field to a pre-heated powder compact. The flow of current through the sample leads to Joule heating, and the negative temperature coefficient of resistivity in the green body induces fast power dissipation and thermal runaway [2, 3, 4, 5]. Compared with conventional sintering, FS has three major significant advantages: lower furnace temperature, faster heating rate and shorter sintering time [2]. These characteristics enable FS to be an energy-saving technique and suitable for preparing fine-grain ceramics [6, 7, 8].

Although FS has attracted world-wide attentions in ceramics research field, it has not been applied to the industrial manufacturing level yet. The key problem of FS is the easy generation of thermal gradients [9, 10, 11, 12], which are closely related to the formation of preferential current paths inside the ceramic sample. Since the sample surface releases heat via thermal radiation during FS [13], the sample surface is much colder than the core region [14, 15, 16]. The hotter region is generally more conductive, resulting in increases of local current density and power dissipation. Consequently, the sample centre becomes much hotter and more conductive, thereby causing local overheating and even the appearance of localised hot paths [6]. A significant thermal gradient is formed between the core and the surface, which is detrimental to the integrated densification and microstructure homogeneity of ceramics [17, 18]. Besides, hot paths are not always formed along the centre-line of the specimen, because the density inhomogeneity in green bodies and poor contact at electrode/ceramic interfaces can also trigger the formation of hot paths away from the centre [2].

Finding technical solutions to eliminate thermal gradients and limit the formation of hot paths during the FS of ceramics has attracted increasing attention. Trombin and Raj et al. reported that the formation of hot paths can be avoided by increasing the furnace temperature, as well as lowering the electric field strength (E) and current density (J) [19]. Other technical solutions like the application of graphite felt sleeve during the flash spark plasma sintering of SiC, and the application of thermally insulating packing powder during the FS of 8YSZ have been proved to be effective in reducing the radiative heat loss from samples and improving the sintered bulk homogeneity correlated to temperature gradients [20, 21]. The application of travelling electrodes during flash sintering could also partially overcome this problem and has been applied to whiteware tiles [22].

The above-mentioned studies were trying to eliminate thermal gradient by optimizing the external environment of samples during FS. However, if the current path can be artificially controlled to avoid the local overheating of ceramic sample during FS, there would be no need to specially adjust the external environment. Inspired by this idea, a new uniform FS method is developed in this study to improve the homogeneity of 3YSZ by current path management. The preferential current path during FS is intentionally shifted from core to near-surface by judicious design of sample geometry and electrode configuration. The concentrated Joule heating near the sample surface can effectively balance the superficial heat loss by radiation, creating a more uniform distribution of temperature inside the sample. Four 3YSZ samples with different geometry and electrode configurations are prepared by flash sintering, and the densification, microstructure, and flexural strength of FSed 3YSZ ceramics are systematically investigated.

The experimental work is supported by direct numerical simulations of the whole

flash sintering process. The numerical approach, based on a Finite Element (FE) multiphysics numerical method, is developed to reproduce the electrical, thermal, and mechanical behavior of 3YSZ during the process.

Several examples of FE models of FS can be found in the literature [23, 24]. For example, numerical models are used in [25] to show that in FS, thermal runaway occurs in the sample with four orders of magnitude higher heating rate compared to conventional sintering, whereas in [16] the electrical resistivity during FS of 3YSZ is investigated. Analogously, in [26], the Finite Element Method (FEM) on a coupled electrothermal nonlinear analysis was used in order to obtain the specimen temperature of 8YSZ after 5 s of flashing. However, these works limit the study to the electrothermal analysis of the phenomenon, thus ignoring the volumetric shrinking of the sample due to the densification of the material during sintering.

Other models, not based on FEM, have been also proposed, e.g. [27] in which the sintering of ceramics under flash sintering is modelled using an approach based on the heat equation coupled with an apparent activation energy kinetic equation for densification. The effect of electric fields on the densification and coarsening of oxide ceramics is still not completely understood, and the mechanisms behind it are still under debate [28, 29]. For these reasons, and possibly because of the computational complexity, no example of FE models of FS simulating the densification of the material could be found in literature. Nonetheless the numerical modelling can prove very effective in understanding and minimizing thermal gradients, which is a crucial aspect for commercialization of the FS technique [25, 29], and in predicting the sintering-related shrinkage.

Contrary to FS, densification models have been thoroughly studied for conventional sintering of ceramics, and several approaches, mostly based on FEM,

have been proposed and compared [30]. Such approaches are generally classified into phenomenological models [31, 32, 33], and physical models [34, 35, 36]. Given the complexity of the phenomena involved, and the limited understanding of the FS process, a phenomenological approach has been adopted for the work presented in this paper. A general equation for the densification is imposed [37, 38, 39], and the related input coefficients are obtained using an optimization procedure similar to the ones suggested by [40] and [41]. The developed multiphysics model is implemented and compared with experimental results, in order to reveal the underlying mechanisms of improved sample homogeneity.

2. Experimental procedure

The starting material was a commercial 3YSZ powder (TZ-3Y-E, Tosoh, Japan), which has a mean particle size of ≈ 60 nm. The maximum density of 3YSZ ceramic sintered from the powder is 6.05 g/cm^3, as provided by supplier. To obtain bar-shape samples, the powder was uniaxially dry-pressed into bars in a steel die at ≈ 60 MPa, followed by cold isostatic pressing at 200 MPa. The as-received bars have a dimension of approximately 30 mm × 6 mm × 3 mm. To make dogbone samples, 3YSZ powder was added to distilled water to give a solid loading of 55wt%, while 2 wt% (relative to the solid) of Dispex A40 was also added as a dispersant. The slurry was prepared with the assistance of ultrasonic dispersion, and then slip cast in dogbone shaped molds on a porous plaster substrate. Dogbone samples were also isostatically pressed at 200 MPa to ensure density uniformity. The as-received dogbone samples have a cross-section of approximately 6 mm × 3 mm as for the bar specimens.

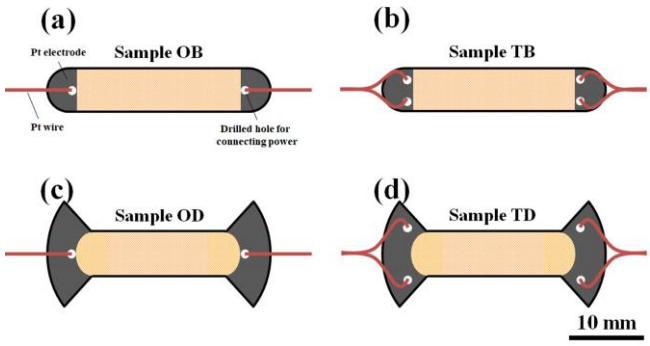

Figure 1: Schematics of the four 3YSZ samples for flash sintering experiments: (a) Sample OB with bar-shape and one drilled hole at each end, (b) Sample TB with bar-shape and two drilled holes at each end, (c) Sample OD with dogbone-shape and one drilled hole at each end, (d) Sample TD with dogbone-shape and two drilled holes at each end. The grey regions represent the Pt paste and the drilled holes are connected to the power supply through Pt wire.

Both the bar and the dogbone samples were pre-heated in an alumina tube furnace in air at 600 ℃ for 1 h to remove the organic ingredients (binder or dispersant). A starting relative density of ≈ 50% was obtained in all the green bodies regardless of sample geometry. All the samples had 1 or 2 holes at both ends with a span of ≈ 23 mm for connections to the power supply. The samples with different geometry and hole number were labeled as Sample OB, TB, OD and TD, as shown in Figure 1. Platinum paste was painted around the ends of specimens intersecting the holes to provide electrodes. The inner surfaces of the holes were also coated with Pt paste.

The green body of each sample was suspended by Pt wires in a box muffle furnace and connected to a commercial DC power source (EA-PS 9360-15, 1500 W, Elektro-Automatik, Viersen, Germany). The data were logged using Labview Software. The furnace was heated to 900 ℃ and held for 10 min to ensure a uniform temperature in the chamber. Subsequently, an initial electric field of 50 V/cm was applied to each sample to trigger flash sintering. The power supply was programmed to apply a constant voltage and then switched automatically to current control when a

current density of 50 mA/mm^2 was reached. The power was turned off after the sample was flash sintered at the target current for 60 s. Videos of the whole processes were taken through a window in the furnace, and used as a validation for the numerical results, as presented in Section 5.

The mean sample temperature during flash sintering is estimated using the non-equilibrium equation of the black-body radiation model [6]:

$$T_s = T_f + \int_0^t \frac{VI - A\sigma\varepsilon\left(T_s^4 - T_f^4\right)}{mC_p} dt \quad (1)$$

where T_s is the sample temperature assuming a uniform temperature throughout the sample, T_f is the furnace temperature, which has a constant value of 1173 K, V is the voltage applied across the sample, I is the current, ε is the emissivity (taken as 0.7 in this work), σ is the Stefan-Boltzmann constant, A is the instantaneous surface area of the light-emitting part of the sample without Pt coating, m is the mass, and C_p is the specific heat (taken as 600 J kg^{-1} K^{-1}) of the 3YSZ sample. It is worth noting that the instantaneous surface A is calculated from the videos.

After flash sintering, the sample ends covered with the Pt coating were cut off to obtain the central cuboid part. Bulk density (ρ) and open porosity (V_{op}) of the remaining samples were measured using the Archimedes displacement method. The density of the fully sintered 3YSZ (ρ_f) was taken as 6.05 g/cm^3 to estimate the relative density by the relation $\rho_* = \rho/\rho_f$.

Cross-sections were cut from the midpoint of the length, polished to 1 μm finish using diamond abrasives, and then thermally etched at 1100 ℃ for 30 minutes. The microstructures of cross-sections (centre and short edge) were observed using scanning electron microscopy (SEM, Merlin-60-62, Zeiss). The mean grain size was estimated from SEM images using the mean linear intercept length. To analyze the flexural strength, bars of 19 mm × 2.8 mm × 2.1 mm were obtained by grinding and

polishing the sample surfaces to 1 μm finish. The three-point bending strength of each sample was measured by a universal tester (Z030TE, Zwick, Germany) using a 15 mm span and a cross-head speed of 0.5 mm/min. A total of 5 bars were tested from each specimen to acquire the mean and standard error of bending strength.

3. Numerical modelling

To analyse the effect of the four different configurations presented in the previous section, a numerical approach to model the entire sintering process is developed and used to simulate the experimental tests presented in the previous section. The size of the gauge sections, i.e. the part of the specimen between the power connection holes, of the four models created is summarised in Table 1.

The model of the sintering process is implemented using the commercial software COMSOL Multiphysics® [42], and includes specific modules already present in the software to model the thermal, electrical, and mechanical behaviour of the specimens. The densification of the material is, instead, reproduced by implementing differential equations linking multiple physics, allowing for the shrinking of the material, as described in detail in the next sections. To the best of the authors' knowledge, the sample densification has never previously been included in numerical models of FS.

3.1. Model formulation

The FE model presented in this paper consists of single integration point pentahedral elements, with a graded element size that is finer around the holes where the gradients are expected to be more significant, as presented in Figure 2. The quality of the elements, expressed in terms of aspect ratio, is presented in the figure, and shows the absence of distorted elements that could affect the accuracy of the

simulations. Additionally, to further improve the quality of the results, second order elements are used for all the modules.

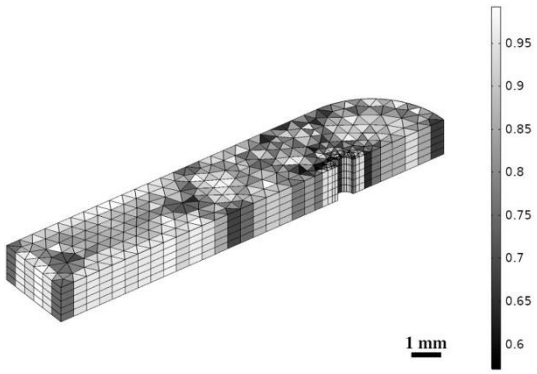

Figure 2: Model of sample OB with symmetries and the grey-scale bar showing the mesh quality.

Table 1: Gauge sections in mm of the four samples

Sample	width × thickness × length (hole-to-hole)
OB	5.84 × 2.66 × 23
TB	5.80 × 2.70 × 24
OD	5.85 × 3.34 × 22
TD	5.92 × 4.04 × 23

Given the symmetry of the specimens along three perpendicular planes, only one eighth of it is modelled, and boundary conditions are imposed to the mid-planes to mimic the presence of the rest of the body, thus reducing the computational cost of the simulations which is particularly demanding for the number of physical processes involved in the model. It is worth noting that the use of symmetry implies that any physical quantity (temperature, density, etc.) does not depend on the different electric polarity of the voltage feed. Although experimental evidence reported in the literature [1] shows that different temperature, and therefore microstructure, can be obtained

near the anode and cathode of FSed specimens subjected to DC voltage, the electrochemical reduction phenomena responsible for this behaviour are ignored in the numerical formulation. This assumption is justified by the limited asymmetry expected in the sintering of the samples used for this work, which was proven by the post-mortem analysis of the samples presented in Section 4.1.

The connection with the power connections was modelled by applying electrical boundary conditions (at first constant voltage and then constant current) to the inner surface of the electrode holes, thus ignoring the presence of Pt paste on the ends of the specimen. Although it is known that the liberal application of Pt paste can reduce the thermal asymmetry between the anode and the cathode [13], since the resistance of the fired paste is much higher than that of the wire a local runaway effect is expected, which would heat up the volume around the hole and induce the current to enter the specimen mainly from the inner surface of the hole. This assumption is supported by the experimental observation that shows a heating hotspot in correspondence of the electrode connection and also by the fact the use of two electrodes rather than one gives clear improvement to the sintering, which would not be the case if the paste were the dominant conduction path.

A set of semi-empirical relationships are introduced to model the variation during the sintering process of certain material properties, from the green body condition (indicated with the subscript g) to the fully sintered material (identified by the subscript f). For sake of conciseness and readability of the equations, the time dependence of the variables is implied.

The material is modelled as a conductive medium with temperature (T) and density (ρ) dependent conductivity. The conductivity σ of the green body and of the fully sintered material are modelled with an Arrhenius law, and the conductivity of

the material is assumed to be the weighted average, with respect to the density, of the values for green body and fully sintered material, i.e.

$$\sigma = \sigma_g e^{-\frac{Q_g}{RT}} + \left(\sigma_f e^{-\frac{Q_f}{RT}} - \sigma_g e^{-\frac{Q_g}{RT}}\right)\left(\frac{\rho-\rho_g}{\rho_f-\rho_g}\right) \quad (2)$$

where σ is the conductivity, and Q is the activation energy. The values for the green body and the fully sintered material are derived from direct experimental measurement, as presented in [16].

As proposed in [43], the thermal conductivity k of the material, instead, is assumed to vary only with the density, following the law:

$$k = k_f \frac{2\rho}{3\rho_f-\rho} \quad (3)$$

As for the electrical conductivity, the values of the thermal conductivity of the green body and the fully sintered material (reported in Table 3) have been measured directly from experiments [43].

Finally, the densification of the material is described with a partial differential equation linking the rate of change of the density with the temperature and instantaneous density:

$$\frac{1}{\rho_*}\frac{\partial \rho_*}{\partial t} = f(\rho_*)g(T) \quad (4)$$

where $f(\rho_*)$ and $g(T)$ are functions of relative density and temperature, respectively, which are derived from the experimental results.

In the literature [38], $f(\rho_*)$ and $g(T)$ are usually of the form:

$$f(\rho_*) = \rho_*^{k_1}\left(\frac{1-\rho_*}{\frac{\rho_g}{\rho_f}-\rho_*}\right)^{k_2} \quad (5)$$

$$g(T) = k_4 T^{k_3} e^{-\frac{-k_5}{RT}} \quad (6)$$

where k_1, k_2, k_3, are integer, possible negative, numbers, whereas k_4 and k_5 are real positive numbers.

Table 2. Values chosen for k_h, with h = 1,⋯ ,5.

k_1	k_2	k_3	k_4	k_5
[−]	[−]	[−]	[$s^{-1}\cdot K^{-1}$]	[J/mol]
0	2	-1	1.25×10^{15}	290×10^{3}

Equations of the type of (5) and (6) are typically derived from physical knowledge of the sintering process or from experimental results. However, given the lack, at the present time, of a sufficient knowledge of the micro-scale flash sintering phenomenon, the constants in (5) and (6) are chosen empirically. Obviously, the choice of (5) affects the choice of (6), and vice-versa. In the literature, for similar problems, optimization algorithms are often used for automatically constructing (5) and (6) to accurately fit the experimental results [41].

In this work, the linear-shrinkage measured from videos of the experiment is used to derive the left-hand-side of (4), and (5) and (6) are chosen accordingly. Obviously, several choices of (5) and (6) are possible. However, some choices of (5) may lead to unrealistic (6), e.g. non-monotonic functions. An optimisation algorithm has been developed to evaluate the best fit of (5) and (6) with the experimental data, as reported in Table 2 for k_h, with $h = 1,\cdots,5$.

Imposing the slight approximation that the mass of the specimen remains unchanged during the sintering process, the increase in density is translated into uniform isotropic shrinkage of the finite element by using the thermal strain multiphysics feature in the "Solid Mechanics" COMSOL module:

$$\varepsilon_t = \left(\frac{\rho_g}{\rho}\right)^{1/3} - 1 \tag{7}$$

where ε_t is the linear thermal strain. The actual values of the relevant material

properties for both the green body and the fully sintered material, derived from direct experimental measurements, are reported in Table 3. Density, conductivity, and activation energy are measured directly from the experiments, and the values of heat conductivity are extracted from [43].

Table 3. Values of the green body and fully sintered material properties used in the numerical models.

State of sample	ρ [kg/m^3]	σ [S/m]	Q [J/mol]	k [W/mK]
Green body	3025	677×10^3	139×10^3	0.4
Fully sintered	6050	37×10^3	96×10^3	2.5

Although the model is phenomenological, the temperature dependence of electrical conductivity and sintering have a physical basis. This allows the comparison of the activation energies for these processes with conventional measurements. The range of activation energies for electric conduction of 96-139 kJ/mol (Q in Table 3) is higher than the activation energy for ionic conductivity under low current density conditions of 77 kJ/mol [44]. The discrepancy is most likely an artefact associated with the electrochemical reduction of the 3YSZ at the high current densities experienced during flash sintering, which is known to increase the conductivity by allowing electronic conduction [16, 45, 46]. The activation energy for densification of 290 kJ/mol (k_5 in Table 2) is significantly lower than the value of 485 kJ/mol reported for conventional sintering of the same powder [47]. This suggests a difference in rate-controlling diffusion mechanism in flash sintering compared with conventional sintering.

3.2. Multiphysics solver

The methodology developed to model the flash sintering of 3YSZ integrates different modules included in the commercial software COMSOL Multiphysics®. The "Electric Currents", "Heat transfer", and "Structural mechanics" modules are used to reproduce, respectively, the electrical, thermal, and mechanical behaviour of 3YSZ prior, during and after the sintering process. Moreover, the multiphysics functionality of COMSOL Multiphysics® is used to link the different physical processes. Additionally, the "Event" and "Global ODEs and DAEs" modules are used to simulate the switch from voltage to current control, reproducing the electrical power supplied to the specimen. Finally, the "Domain ODEs and DAEs" module is used to model the change in density (and in volume) of the specimen, by implementing (4) as a user defined differential equation.

The material models and boundary conditions described in the previous section are implemented in the corresponding modules, and a segregated solver is set up to solve sequentially the different physical processes by means of the iterative scheme shown in Figure 3. At each internal step, an implicit problem is set up and the resulting system of equations is solved by using non-linear solvers and preconditioned iterative solution strategies.

The time stepping is adaptive and, in order to avoid the propagation of numerical issues, a small tolerance value of 10^{-6} is chosen for the stopping criterion. The minimum time step taken by the solver is $\sim 2\times10^{-5}$ s, close to the switch from voltage to current control (i.e. close to the flash event), whereas the maximum time step is 0.5 s. Thanks to the adaptive time-stepping, each internal step required fewer than 10 iterations, depending on the distance in time from the flash. Analogously, the general multiphysics step also required fewer than 20 iterations for each time step. The whole simulation of each sample requires about 30 min. Computation timings are given with

respect to a machine equipped with 6-core/24-thread processors (Xeon E5645 at 2.40 GHz) and 104 GB of RAM running Windows.

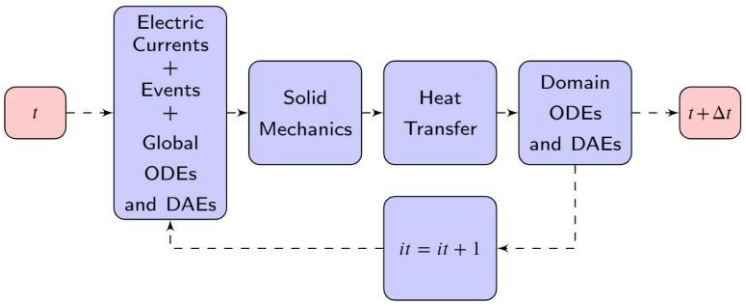

Figure 3: Segregated solver scheme: the physical processes are solved in four internal steps, which are repeated until the global tolerance is under 10^{-6}. The time step Δt is adaptively chosen by the solver.

Table 4. Steady-state temperature, density, open porosity, mean grain size and flexural strength of the four FSed 3YSZ samples. Steady state temperature is evaluated from Eq. (1) and other results are derived from experiments.

Sample	Steady-state temperature [K]	Relative density [%]	Open porosity [%]	Mean grain size (core) [μm]	Mean grain size (surface) [μm]	Flexural strength [MPa]
OB	1598	92.7	4.2	167	80	1203 ± 17
TB	1643	96.0	1.9	148	92	1336 ± 19
OD	1628	95.5	2.4	157	83	1258 ± 16
TD	1658	99.7	0.2	137	111	1501 ± 15

4. Results

In this section, the outcomes of the experimental tests are analysed and compared against the numerical results, to identify the effect of the individual features on the property of the sintered material. First, the results of the FS experiments are compared to highlight the difference between the four specimen configurations, in terms of final

density, microstructure topology, and mechanical properties of the material. The results of the numerical simulations are then analysed, and validated against the directly measured quantities during the flash sintering process as well as with the final properties of the material.

4.1. Experimental results

The relative densities and open porosities of 3YSZ samples after flash sintering are listed in Table 4. It can be seen that increasing the number of power connection points and the replacement of bar-shape by dog-bone shape were effective in making the sample denser and less porous. Compared with Sample OB, the relative density was particularly improved by 7% in Sample TD. To the best of our knowledge, it proves for the first time that the densification efficiency of FS can be improved by simply acting on the sample geometry and electrode configuration.

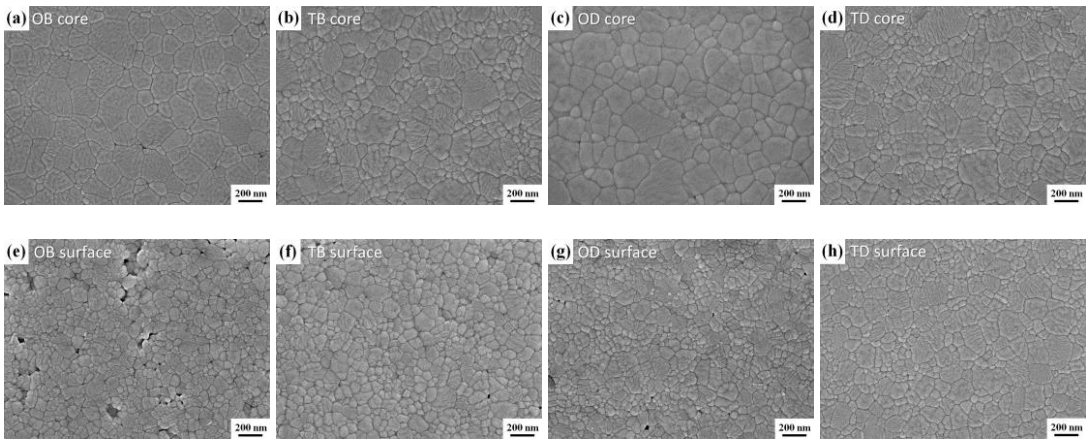

Figure 4: SEM images of the polished and thermally etched cross-sections from core (top row) and surface (bottom row) of 3YSZ sample: (a, e) Sample OB, (b, f) Sample TB, (c, g) Sample OD, (d, h) Sample TD.

The SEM micrographs in Figure 4 show clearly the different microstructural characteristics from the core and the surface of flash sintered samples. The central

regions were dense in all samples and the mean grain size was in the order of OB>OD>TB>TD as shown in Figure 4(a–d). However, as estimated by the black-body radiation model, the sample temperature was in the order of TD>TB>OD>OB, which is reverse to the order of mean grain size.

Different extents of core/surface microstructural gradient can be found in all 3YSZ samples, which can be attributed to the heat loss at the sample surfaces during flash sintering. The surface of conventionally flashed sample (OB) was found to have high porosity and small grains in Figure 4(e). Increasing the number of power-connection holes [Sample TB, Figure 4(f)], or the replacement of bar by dogbone geometry [Sample OD, Figure 4(g)], was found to be effective in decreasing porosity and increasing grain size of the surface areas. When both of the two modifications were applied, a pore-free microstructure was successfully obtained at the surface of Sample TD [Figure 4(h)]. Moreover, the mean grain size of the surface (111 μm) was very close to that of the core region (137 μm) in Sample TD, indicating a fairly low extent of microstructure gradient. Therefore, it is demonstrated that the application of dogbone geometry, forked electrodes, and cross section aspect ratio effectively improved the density and microstructural homogeneity of 3YSZ samples.

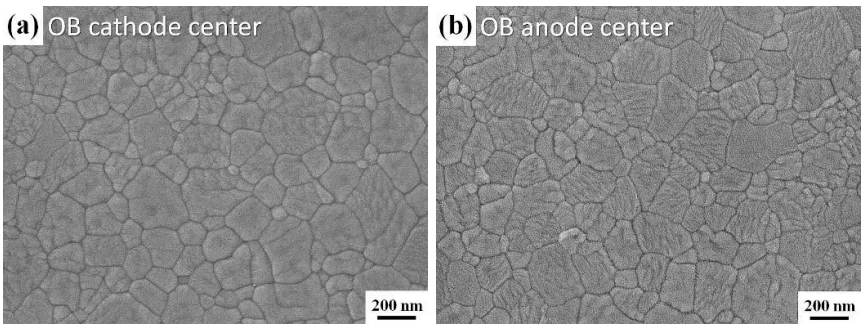

Figure 5: SEM images of the polished and thermally etched cross-section centers from (a) cathode and (b) anode of Sample OB after flash sintering.

The SEM images of the cross-section centers from the cathode and the anode of Sample OB are shown in Figure 5. There is no significant difference in the microstructures near the electrodes, with the mean grain sizes of cathodic and anodic centers, measured from Figure 5(a) and (b), equal to 168 μm and 165 μm, respectively. Moreover, the microstructures at the electrodes are similar to that of the core region of Sample OB in Figure 4(a). Similar behaviour is observed also in the other 3YSZ samples (TB, OD and TD) and could mainly be attributed to two reasons: first, a generous coat of Pt paste was applied at the ends of 3YSZ samples to form high-quality electrodes, which mitigated the contact resistance at electrodes and the thermal asymmetry from cathode to anode [13]. Second, a moderate current density of 50 mA/mm^2 and a short sintering time of 60 s were used to flash sinter the 3YSZ samples, which alleviated the electrochemical reduction at the cathode. Therefore, the asymmetry of FSed 3YSZ samples was not evident in this study. The systematic investigation on mitigating microstructure asymmetry from cathode to anode will be carried out in the future.

The three-point bending strengths of flash sintered 3YSZ samples are also shown in Table 4, and all the samples exhibit high strengths of ≥ 1200 MPa. It was evident that the increased number of power connection points and the replacement of bar-shape by dogbone-shape were beneficial for improving the strength of 3YSZ sample. Notably, Sample TD possessed a very high strength of 1501±15 MPa, showing a significant increase of ≈ 25% compared to 1203±17 MPa for Sample OB. Furthermore, the standard deviations of strength from which the standard errors shown in Table 4 are derived were only ~3%. This very high reliability of the strength corresponds to Weibull moduli ≥ 40. The smaller grain size in the core region, lower porosity at surface, and improved core/surface microstructural homogeneity are

considered to be responsible for the increase of the strength of 3YSZ ceramic. This result clearly demonstrated that uniform flash sintering could further enhance the mechanical properties of 3YSZ ceramic.

4.2. Simulation results

The experimentally measured dimensions of the specimens presented in section 2 were used to generate FE models of each of the four tests.

To mimic the voltage source imposed during the experimental test, a variable electric potential was introduced between the surface of the hole and the symmetry plane perpendicular to the length of the specimen. To fully mimic the electrical load applied during the experimental tests, the difference of potential was kept constant during the voltage controlled regime, and then varied to impose constant current once the critical value of current for the specific sample was reached, which corresponds to an average current density of 50 mA/mm^2 in the green body.

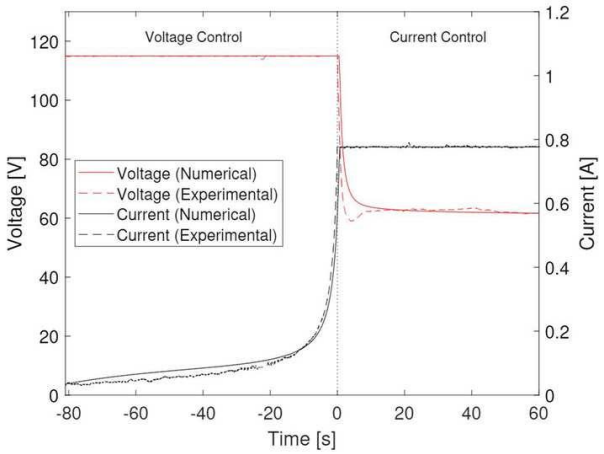

Figure 6: Validation of voltage (red) and current (black) numerical predictions (solid line) against experimental measures (dashed line) during the FS of sample OB. The critical instant for the transition from voltage to current control was defined as t = 0 s.

To validate the numerical results, the evolution of current and difference of

potential during the simulation have been compared against the experimental values directly measured during the sintering process showing excellent agreement. Figure 6 shows the comparison between numerical and experimental measurements for the sample OB. Similar curves, with comparable level of agreement were obtained for the other three samples (DB, OD, and TD).

Additionally, the densification predicted with the numerical models is compared against the evolution of the density evaluated from measuring the shrinkage of the specimens. The length of the top and bottom edges of the samples have been measured from the snapshots of videos of the experiments, with a frequency of 1 s^{-1}. The density for each measurement has been calculated assuming uniform and isotropic deformation of the specimen as:

$$\rho = \rho_g \left(\frac{L_g}{L}\right)^3 \tag{8}$$

where ρ_g and L_g are the density and the length of the green body specimens, respectively.

The values of the densities evaluated using the measure of top and bottom edge of the specimen provide an estimate of the experimental scatter, which takes into account the asymmetry of the deformation observed during some tests. The rapid changes of camera exposure during the video due to the sudden variation of brightness during the test hinder the accuracy of the length measurements, which is taken into account by adding a 1% error to the value of L. The maximum and minimum values of the density evaluated for each video frame constitute the limits of the experimental scatter.

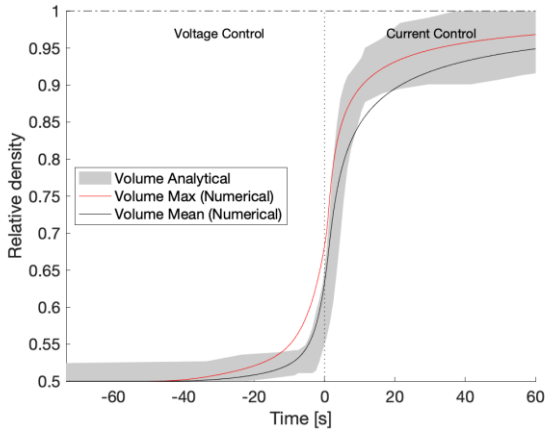

Figure 7: Comparison of the density evaluated from experimental estimation (grey area) against numerical prediction of the average (black) and maximum (red) density for the OB specimen.

The comparison of the density evaluated numerically (solid lines) and experimentally (grey area) for sample OB is presented in Figure 7. The red line represents the maximum value of the density, measured in the centre of the numerical model, at each time step. The black line instead represents the mean density evaluated in the volume between the holes, which in the experimental tests would not be covered by Pt paste. The curve of the numerically predicted mean density falls almost entirely within the scatter of experimental values represented by the gray area, showing excellent agreement between the simulations and the experiments. The numerical models seem to predict a more gradual evolution of the density than the experiments suggest, but the slight mismatch can be due to the already mentioned sudden change in brightness during the flash event, which affects the accuracy of the specimen length measurements at the beginning and the end of the flash. Similar results, and comparable level of agreement, are also obtained for samples TB, OD and TD.

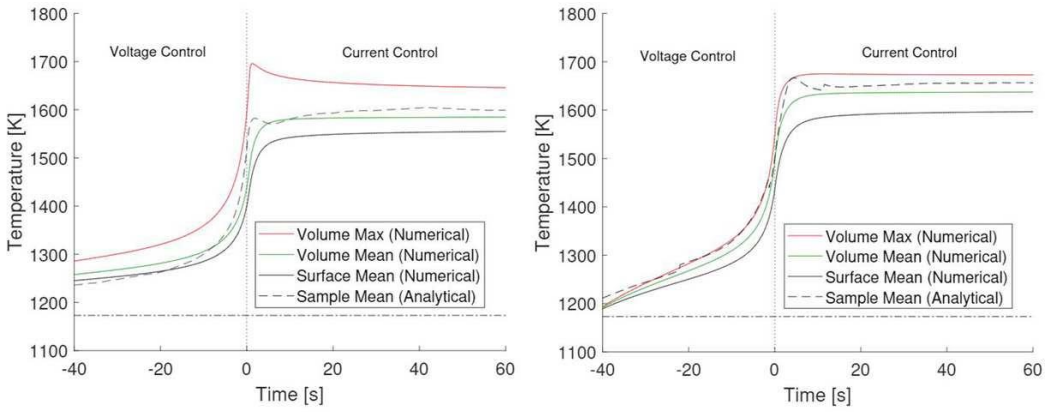

(a) OB temperature profile (b) TD temperature profile

Figure 8: Comparison of the sample mean temperature evaluated from experimental data by using the black-body radiation model as (calculated using Eq. (1)) against numerical prediction of the temperature (surface mean, volume mean, and volume maximal) for the OB and TD specimens.

Table 5. Temperatures predicted by the numerical model both overall and at the steady state compared against the sample mean temperature derived from experimental data ($T^s_{\mathrm{mean-exp}}$), using the black-body radiation model Eq. (1). Results are in *K*.

–	OB	TB	OD	TD
T^s_{mean} (Steady state)	1554	1568	1579	1596
T^v_{max} (Steady state)	1645	1650	1658	1680
T^v_{mean} (Steady state)	1585	1608	1615	1637
$T^v_{\mathrm{max-t}}$ (Overall)	1696	1657	1670	1681
$T^v_{\mathrm{max-t}} - T^v_{\mathrm{mean}}$	111	49	55	44
$T^s_{\mathrm{mean-exp}}$ (Steady state)	1600	1642	1644	1658

Figure 8 shows temperature (surface mean, volume mean, and volume maximum) evaluated numerically and compared against the surface mean temperature derived from experimental data using equation (1). As can be seen, the numerical and

analytical surface mean temperatures differ by about 50 K at the end of the transient. The simplistic assumption of single equivalent temperature leads to an overestimation of the temperature evaluated by (1). This results in T_s being greater that the actual average surface temperature of the sample. Approximations of the analytical approach (1) include the neglect of heat loss from the centre of the sample to the ends, beyond the electrodes, and to the wires supplying the current. Similar results, and comparable levels of agreement, were also obtained for samples TB and OD. The steady-state and the maximum temperatures predicted by the numerical model are reported in Table 5 alongside the surface temperature derived from experimental data using the black-body radiation model defined by (1). Additionally, the difference between the overall maximum temperature and the steady state mean temperature is reported in the table as a qualitative measure of the temperature homogeneity in the samples.

Table 6. Comparison of experimentally measured and numerically predicted relative density of the four specimens.

−	OB	TB	OD	TD
Experimental	92.7%	96.0%	95.5%	99.7%
Numerical	93.5%	95.6%	95.1%	97.7%
Error	0.8%	0.4%	0.5%	1.9%

Table 6, instead, shows the final average densities for the four samples predicted by the numerical model and compared with the experimental values. As can be seen, the agreement is quite good, with the difference well below 1% for the samples OB, TB, and OD, and less than 2% for the sample TD.

Table 7. Fraction of the gauge volume with relative density higher than 95% for the four numerical models. The gauge volume was defined as the part of the sample between the drilled holes at the ends.

–	OB	TB	OD	TD
Volume Fraction	40%	65%	60%	85%

Finally, Table 7 shows the percent of the gauge section volume that has reached a high level of densification ($\rho_* \geq 95\%$) for the four samples. The gauge volume is defined as the part of the sample between the drilled holes at the ends. The results further prove the efficacy of the combination of forked electrodes with the dogbone shape on the densification of 3YSZ sample.

It is worth noting that the higher mismatch observed for the sample TD is due to the simplistic nature of the equation use to define $f(\rho*)$ in (5), which does not include the effect of the stress gradients due to different sintering level. As the inner part of the specimen starts to sinter, the cold parts on the outside experience a compressive stress state, which should help the surface region to densify, which might be one reason why the experimental densities are slightly higher.

Modelling of traditional sintering often adopts piece-wise defined functions for $f(\rho*)$, with different sets of parameters for different density ranges [48]. In particular, numerical models of traditional sintering impose different behaviour of $f(\rho_*)$ for $\rho_* > 90\%$, allowing for higher densification rate and density values than (5). However, given the limited knowledge of the micromechanical behaviour of 3YSZ during flash sintering, in this work a single set of parameters is adopted for all the densities, thus avoiding the introduction of artificial adjustments that cannot be reasonably justified.

The validations presented show the high level of accuracy of the numerical

simulations, which are demonstrably able to reproduce the electrical response of the material during the sintering process as well as the densification process. This provides the confidence of using the numerical simulations to analyse the behaviour of the inner part of the specimen, and to explore the evolution of parameters within the whole volume, which would be extremely challenging to directly measure during the experimental test.

In particular, the numerical predictions of the distribution of current density, temperature, and density within the whole specimen volume are used to explain the possible reasons for the different behaviour of the four configurations analysed in this paper, as presented in the next section.

5. Discussion

The experimental results presented in this study demonstrate that the uniformity of flash sintering can be effectively improved by a rational design of the sample geometry and electrode configuration.

From the experimental results summarised in Table 4, the four configurations analysed lead to very different grain size distributions in the specimens, both in terms of absolute value and gradient between the core and the outer surface of the samples. Specifically, the OB specimen shows the highest grain size in the core, with the smallest grain size on the outer surface, which is compatible with the models that show that OB sample exhibits the highest temperature peak along the centreline at the flash (visible in Figure 8(a)) combined with a steep temperature gradient towards the outer surface. A similar pattern is shown in the sample OD, as the presence of the single power connection point at each end focuses the current density (and therefore the temperature) along the centreline of the specimen, although the combination of

dogbone shape and different cross-sectional dimensions reduces slightly the gradient between the core and the surface of the specimen. It is worth noting that the uniformity of the temperature distribution predicted by the numerical model (see Figure 8 and Table 5) can be ranked as TD>TB>OD>OB which is coherent with the uniformity of the grain size distribution measured in the four samples (see Table 4).

The absence of a temperature peak at the flash in the TB and TD samples, due to a more uniform current density within the gauge section, leads to a more uniform grain size distribution. The dogbone sample shows again a positive effect on the homogeneity of the microstructure, as a combination of thicker sample and large extremities with more widely separated power connections.

The use of numerical models allows monitoring of the evolution of material parameters within the volume, linking the different final properties of the material to specific features of the specimen design. By analysing the current density in the four configurations, for example, it was possible to observe how the same electric potential generates very different current paths, as graphically shown by the current density isosurfaces presented in Figure 9. The distribution of current density streamlines in the four models at the end of the sintering is significantly influenced by the design of the specimen. The use of two power connection points per side in the configurations TB and TD produces a wider and more uniform current density across the gauge section, contrary to what happens in the specimens OB and OD, in which the position of the electrode on the plane of symmetry induces the current to flow along the region close to the central axis of the structure. Additionally, the presence of the large extremities and thicker cross section in the dogbone samples contributes to making the current density within the gauge section more uniform than in the corresponding straight configuration. To decouple the effect of the dogbone shape from the specimen

thickness, numerical simulations of the OD and TD designs with the same dimensions as OB and TB, respectively, were performed. The simulations showed that the aspect ratio of the cross section plays an important role in the uniformity of the current density (and consequently temperature and density) for all the specimens, with the homogeneity improving as the aspect ratio approaches 1. The large extremities, instead provide a minor effect on the current path for the OD specimen, leading to a slightly more uniform current distribution in the cross section. For the specimen TD the effect of the large extremities is significant, as it allows the spacing of the electrodes to be larger than the actual cross section.

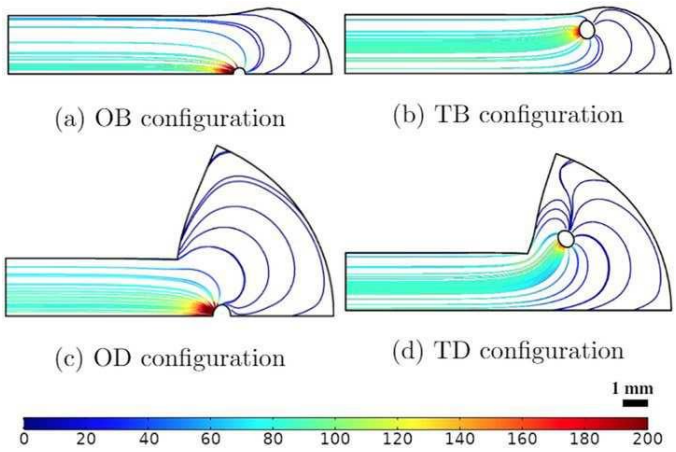

Figure 9: Current density streamline (in mA/mm^2) in four 3YSZ samples at the end of FS analysed by the numerical model.

Following a similar pattern as the density of current, the temperature distribution in the gauge section is more uniform in the dogbone samples, as shown in Figure 10. As a combination of all the effects described, the current density is mostly concentrated in the center for the sample OB, shifting slightly towards the edge in the sample OD. Similar behaviour can be observed in the configurations TB and TD, in this case enhanced by the increased distance between the power connection holes and

the centreline of sample TD.

The different current density distributions lead to different temperature distributions, which in turn affect the densification process of the specimen, as shown in Figures 10 and 11, respectively.

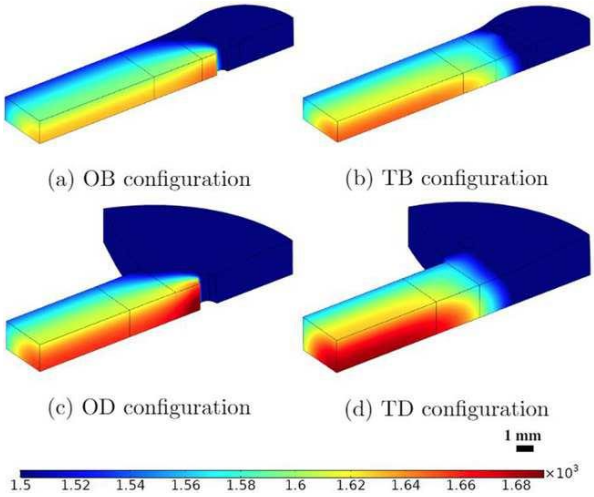

Figure 10: Temperature distribution (in K) in four 3YSZ samples at the end of FS analysed by the numerical model.

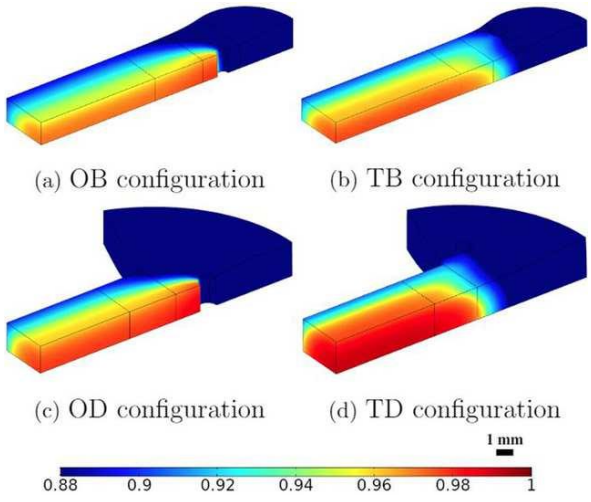

Figure 11: Relative density distribution in four 3YSZ samples at the end of FS analysed by the numerical model.

The figure shows that also the number of holes for the electrodes is extremely

significant, as the presence of two holes, away from the longitudinal axis of the specimen, provides a more uniform Joule heating in the gauge section, and consequently a more homogeneous temperature distribution in the cross section, than the configuration with only one hole per side. Increasing the number of holes has also the effect of reducing the current density close to the electrodes, thus lowering the temperature on the hole predicted by the numerical models. The reduction of the current density concentration close to electrodes also alleviates the adverse effect of the contact resistance between the electrode and the specimen, which is suspected to be one of the main sources of uncertainty in the experimental results. Given its unpredictable nature, the contact resistance was not considered in the numerical models, however the relatively good agreement between the experimental and numerical results indicates that the presence of the Pt paste reduced the overall influence of the contact resistance on the sintering process.

The uniformity of density predicted by the numerical models is in agreement with the experimental observations of grain size distribution in the cross sections presented in Figure 4. As a consequence of the higher densification and more homogeneous grain size distribution, the flexural strength of 3YSZ ceramic was greatly increased from 1203 ± 17 MPa for the bar specimen with one electrode hole per end (OB) to 1501 ± 15 MPa for the dogbone specimen with two holes at each end (TD), as presented in Table 4.

The evolution of the temperature and density across the flash event for the OB and TD specimens are graphically summarised in Figures 12 and 13. In the graphical summary three snapshots of the specimen during the experimental test - before, during, and after the flash event - are compared against the contour plots of temperature (top row) and relative density (bottom rows) predicted numerically at the

same times. Additionally, the vertical grey lines show visually the good agreement in the prediction of the specimen length during the sintering process described by Figure 7. The visual comparison of the experimental behaviour against the numerical prediction of the specimens offers the possibility to analyse local behaviours.

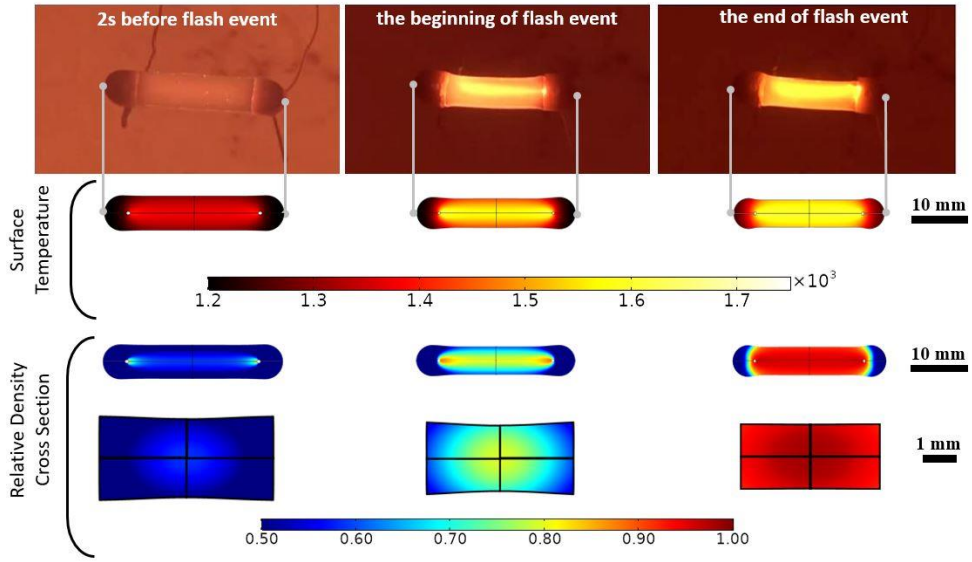

Figure 12: Snapshots of the OB specimen at 2 s before, at the beginning and at the end of flash event, alongside the corresponding numerical predictions of surface temperature and relative density.

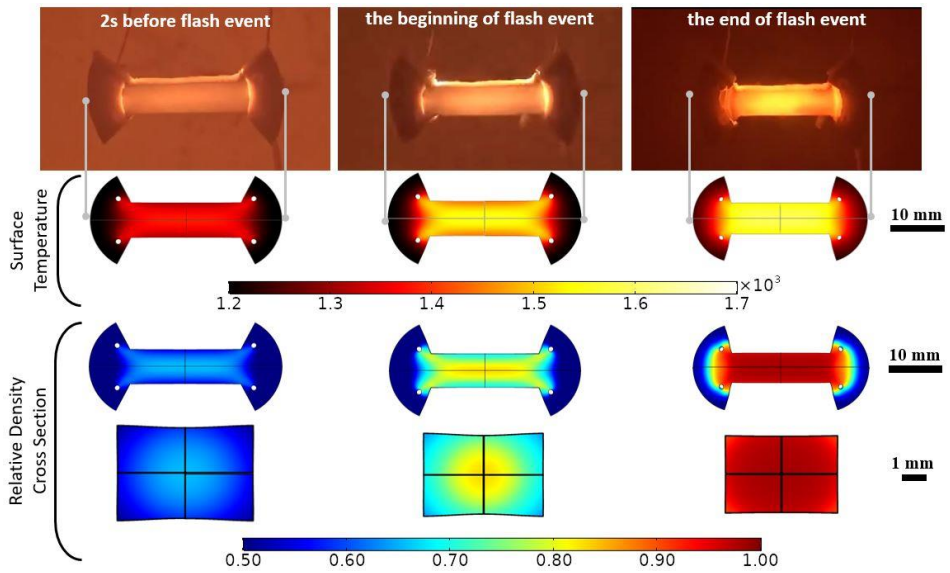

Figure 13: Snapshots of the TD specimen at 2 s before, at the beginning and at the end of flash event, alongside the corresponding numerical predictions of surface temperature and relative density.

Besides the already discussed temperature and densification localisation along the centreline, other localised behaviours can be observed in the pictures of the experimental test, such as the slight bending of the specimen during the flash event and the localised temperature peaks around the electrodes. These features are due to the non-ideal nature of the contact between the electrode and the material. The non-uniform contact between the inner surface of the hole and the specimen leads to a slight bending of the specimen across the flash event, as the portion of specimen between the actual contact points sinters faster than the rest of the volume. Additionally, the contact resistance between the electrode and the specimen induces localised heating of the material which leads to the bright temperature peaks visible in the experimental test. Neither of these phenomena are reproduced by the numerical model, as the electrodes are imposed to be in contact with the inner surface of the hole and without any contact resistance. The good agreement between the experimental and numerical results suggests that the contact imperfections have little influence on the overall flash sintering process. Nonetheless, the outcome of this work will help designing improved configurations of flash sintering tests, with limited contact effects, in future projects.

Figure 13 shows a similar comparison between photos of the sample before, during, and after the flash event and the corresponding contour plot of temperature and density predicted by the numerical model for the TD specimen. As for the OB specimen, the prediction of the specimen length across the flash event is quite accurate, as the qualitative temperature pattern. The localised phenomena observed in the OB specimen, due to non-ideal nature of the contacts, are very limited in the TD configuration, as the presence of two electrode holes per side, combined with the large extremities and the higher thickness of the specimen, reduce the contact

resistance and limits the asymmetry of the sintering process.

6. Conclusions

In this paper, four different specimens for the flash sintering of 3YSZ samples are compared. The combination of two shapes (straight and dogbone) and two electrode connections (one or two holes per side) allowed the generation of four configurations that have noticeably different flash sintering behaviours, both in terms of final average density as well as of uniformity of densification within the cross section. Specifically, the presence of two holes proves to be extremely beneficial as it leads to an increase of the final density with respect to the same shape with a single hole. The configuration with two holes shows also a significant reduction of the grain size gradient between the core and the surface of the specimen, leading to a much more uniform microstructure than the one obtained with the corresponding samples with a single hole.

The shape of the specimen is also proved to influence the final density of the material, both in terms of mean value, as well as in terms of uniformity within the cross section. Specifically, the dogbone shaped specimens reached higher and more uniform density than the corresponding straight specimens with the same number of holes for the electrodes.

The effect of the shape is comparable to the effect of the number of electrodes, leading to the dogbone specimen with two electrode holes per side to reach the highest, i.e. 99.7% density and flexural strength of 1501±15 MPa with the most uniform grain size distribution among the samples presented in this paper.

To explore the reasons behind the different behaviours, a numerical model of each of the specimens was built. A constitutive model, able to accurately predict the

electrical, thermal, and mechanical behaviour of the material has been developed, and used to simulate the sintering of the four different specimen configurations. The numerical simulations allow for understanding how the shape and the number of electrode holes affect the current path, which in turn leads to different temperature distributions and densification patterns. The simulations show how the dogbone shape, with its larger extremities, leads to a more uniform current density within the gauge section, which induces a more homogeneous densification.

The approach presented in this paper, based on the combination of experimental tests and numerical simulations allows the exploration of the effect of the different specimen configurations, to identify the best design among the ones considered, and to analyse the reasons behind the different sintering outcomes. Additionally, the comparison of experimental and numerical results also allows for identifying the limitations of the experimental setup, highlighting the difference between the real behaviour and the idealised configuration, thus helping further to improve the specimen design. From the authors' perspective, the proposed multiphysics numerical model of FS can be seen as a first attempt of including electrical, thermal, and mechanical physics and it can help in overcoming crucial obstacles for commercialization of the FS technique, such as the thermal gradients, by investigating different electrical excitation, number and arrangement of electrodes, and electrical control strategies.

Future investigations will focus on the improvement of the numerical model in order to enhance its accuracy also for higher level of densification, therefore a more precise model for the densification rate will be investigated.

7. Acknowledgements

Dr. Yinsheng Li appreciates the financial support from 3315 Innovation Team Program of Ningbo (Grant no. Y81411DL03).

References

[1] M. Cologna, B. Rashkova, R. Raj, Flash sintering of nanograin zirconia in <5 s at 850 °C, Journal of the American Ceramic Society 93 (11) (2010) 3556–3559. doi:10.1111/j.1551-2916.2010. 04089.x.

[2] M. Biesuz, V. M. Sglavo, Flash sintering of ceramics, Journal of the European Ceramic Society 39 (2) (2019) 115–143. doi:10.1016/j.jeurceramsoc.2018.08.048.

[3] R. Raj, Joule heating during flash-sintering, Journal of the European Ceramic Society 32 (10) (2012) 2293–2301. doi:10.1016/j.jeurceramsoc.2012.02.030.

[4] M. Yu, S. Grasso, R. Mckinnon, T. Saunders, M. J. Reece, Review of flash sintering: materials, mechanisms and modelling, Advances in Applied Ceramics 116 (1) (2017) 24–60. doi:10.1080/17436753.2016.1251051.

[5] R. I. Todd, E. Zapata-Solvas, R. S. Bonilla, T. Sneddon, P. R. Wilshaw, Electrical characteristics of flash sintering: thermal runaway of joule heating, Journal of the European Ceramic Society 35 (6) (2015) 1865–1877. doi:10.1016/j.jeurceramsoc.2014.12.022.

[6] W. Ji, B. Parker, S. Falco, J. Zhang, Z. Fu, R. I. Todd, Ultra-fast firing: Effect of heating rate on sintering of 3YSZ, with and without an electric field, Journal of the European Ceramic Society 37 (6) (2017) 2547–2551. doi:10.1016/j.jeurceramsoc.2017.01.033.

[7] W. Ji, J. Zhang, W. Wang, Z. Fu, R. I. Todd, The microstructural origin of rapid densification in 3YSZ during ultra-fast firing with or without an electric field, Journal

of the European Ceramic Society 40 (15) (2020) 5829–5836. doi:10.1016/j.jeurceramsoc.2020.07.027.

[8] Y. Dong, H. Wang, I.-W. Chen, Electrical and hydrogen reduction enhances kinetics in doped zirconia and ceria: I. grain growth study, Journal of the American Ceramic Society 100 (3) (2017) 876–886. doi:10.1111/jace.14615.

[9] W. Qin, J. Yun, A. M. Thron, K. van Benthem, Temperature gradient and microstructure evolution in ac flash sintering of 3 mol% yttria-stabilized zirconia, Materials and Manufacturing Processes 32 (5) (2017) 549–556. doi:10.1080/10426914.2016.1232814.

[10] D. Demirskyi, O. Vasylkiv, Hot-spots generation, exaggerated grain growth and mechanical performance of silicon carbide bulks consolidated by flash spark plasma sintering, Journal of Alloys and Compounds 691 (2017) 466–473. doi:10.1016/j.jallcom.2016.08.234.

[11] Y. Dong, On the hotspot problem in flash sintering (2017). arXiv:1702.05565.

[12] G. M. Jones, M. Biesuz, W. Ji, S. F. John, C. Grimley, C. Mani` ere, C. E. J. Dancer, Promoting microstructural homogeneity during flash sintering of ceramics through thermal management, MRS Bulletin 46 (1) (2021) 59–66. doi:10.1557/s43577-020-00010-2.

[13] M. Biesuz, L. Pinter, T. Saunders, M. Reece, J. Binner, V. M. Sglavo, S. Grasso, Investigation of electrochemical, optical and thermal effects during flash sintering of 8YSZ, Materials (Basel, Switzerland) 11 (7) (2018) 1214. doi:10.3390/ma11071214.

[14] I. J. Hewitt, A. A. Lacey, R. I. Todd, A mathematical model for flash sintering, Mathematical Modelling of Natural Phenomena 10 (6) (2015) 77–89. doi:10.1051/mmnp/201510607.

[15] S. Grasso, Y. Sakka, N. Rendtorff, C. Hu, G. Maizza, H. Borodianska, O.

Vasylkiv, Modeling of the temperature distribution of flash sintered zirconia, Journal of the Ceramic Society of Japan 119 (1386) (2011) 144–146. doi:10.2109/jcersj2.119.144.

[16] M. Yoshida, S. Falco, R. I. Todd, Measurement and modelling of electrical resistivity by four-terminal method during flash sintering of 3YSZ, Journal of the Ceramic Society of Japan 126 (7) (2018) 579–590. doi:10.2109/jcersj2.17256.

[17] Y. Du, A. J. Stevenson, D. Vernat, M. Diaz, D. Marinha, Estimating joule heating and ionic conductivity during flash sintering of 8YSZ, Journal of the European Ceramic Society 36 (3) (2016) 749–759. doi:10.1016/j.jeurceramsoc.2015.10.037.

[18] M. C. Steil, D. Marinha, Y. Aman, J. R. Gomes, M. Kleitz, From conventional ac flash-sintering of YSZ to hyper-flash and double flash, Journal of the European Ceramic Society 33 (11) (2013) 2093–2101. doi:10.1016/j.jeurceramsoc.2013.03.019.

[19] F. Trombin, R. Raj, Developing processing maps for implementing flash sintering into manufacture of whiteware ceramics, American Ceramic Society Bulletin 93 (2014) 32–35.

[20] S. Grasso, T. Saunders, H. Porwal, B. Milsom, A. Tudball, M. Reece, Flash spark plasma sintering (fsps) of α and β sic, Journal of the American Ceramic Society 99 (5) (2016) 1534–1543. doi:10.1111/jace.14158.

[21] M. Biesuz, J. Dong, S. Fu, Y. Liu, H. Zhang, D. Zhu, C. Hu, S. Grasso, Thermally-insulated flash sintering, Scripta Materialia 162 (2019) 99–102. doi:10.1016/j.scriptamat.2018.10.042.

[22] E. Sortino, J.-M. Lebrun, A. Sansone, R. Raj, Continuous flash sintering, Journal of the American Ceramic Society 101 (4) (2018) 1432–1440. doi:10.1111/jace.15314.

[23] X. Li, R. Huang, X. Wang, G. Liu, Z. Jia, L. Wang, A simple optimized design

of an electrode to conduct flash sintering at room temperature and low onset electric field, Scripta Materialia 186 (2020) 158–162. doi:10.1016/j.scriptamat.2020.05.024.

[24] A. Eqbal, K. S. Arya, T. Chakrabarti, In-depth study of the evolving thermal runaway and thermal gradient in the dog bone sample during flash sintering using finite element analysis, Ceramics International 46 (8, Part A) (2020) 10370–10378. doi:10.1016/j.ceramint.2020.01.034.

[25] A. Eqbal, K. S. Arya, T. Chakrabarti, In-depth study of the evolving thermal runaway and thermal gradient in the dog bone sample during flash sintering using finite element analysis, Ceramics International 46 (8, Part A) (2020) 10370–10378. doi:10.1016/j.ceramint.2020. 01.034.

[26] J. G. Pereira da Silva, J.-M. Lebrun, H. A. Al-Qureshi, R. Janssen, R. Raj, Temperature distributions during flash sintering of 8% yttria-stabilized zirconia, Journal of the American Ceramic Society 98 (11) (2015) 3525–3528. doi:10.1111/jace.13786.

[27] J. G. P. da Silva, H. A. Al-Qureshi, F. Keil, R. Janssen, A dynamic bifurcation criterion for thermal runaway during the flash sintering of ceramics, Journal of the European Ceramic Society 36 (5) (2016) 1261–1267. doi:10.1016/j.jeurceramsoc.2015.11.048.

[28] C. Cao, R. Mücke, O. Guillon, Effect of ac field on uniaxial viscosity and sintering stress of ceria, Acta Materialia 182 (2020) 77–86. doi:10.1016/j.actamat.2019.10.035.

[29] J. V. Campos, I. R. Lavagnini, J. G. Pereira da Silva, J. A. Ferreira, R. V. Sousa, R. Mücke, O. Guillon, E. M. Pallone, Flash sintering scaling-up challenges: Influence of the sample size on the microstructure and onset temperature of the flash event, Scripta Materialia 186 (2020) 1–5. doi:10.1016/j.scriptamat.2020.04.022.

[30] V. N. Chung, S. S. Koundinya, V. K. Stanley, G. N. Anh, A. Bezold, C. Broeckmann, F. Lange, A comparative study of different sintering models for al2o3, Journal of the Ceramic Society of Japan 124 (4) (2016) 301–312. doi:10.2109/jcersj2.15257.

[31] E. A. Olevsky, Theory of sintering: from discrete to continuum, Materials Science and Engineering: R: Reports 23 (2) (1998) 41–100. doi:10.1016/S0927-796X(98)00009-6.

[32] M. Abouaf, J. L. Chenot, G. Raisson, P. Bauduin, Finite element simulation of hot isostatic pressing of metal powders, International Journal for Numerical Methods in Engineering 25 (1) (1988) 191–212. doi:10.1002/nme.1620250116.

[33] A. Al-Qudsi, M. Kammler, A. Bouguecha, C. Bonk, B.-A. Behrens, Comparison between different numerical models of densification during solid-state sintering of pure aluminium powder, Production Engineering 9 (1) (2015) 11–24. doi:10.1007/s11740-014-0574-7.

[34] H. Riedel, J. Svoboda, A theoretical study of grain growth in porous solids during sintering, Acta Metallurgica et Materialia 41 (6) (1993) 1929–1936. doi:10.1016/0956-7151(93)90212-B.

[35] J. Svoboda, H. Riedel, H. Zipse, Equilibrium pore surfaces, sintering stresses and constitutive equations for the intermediate and late stages of sintering—i. computation of equilibrium surfaces, Acta Metallurgica et Materialia 42 (2) (1994) 435–443. doi:10.1016/0956-7151(94) 90498-7.

[36] T. Kraft, H. Riedel, Numerical simulation of solid state sintering; model and application, Journal of the European Ceramic Society 24 (2) (2004) 345–361, 8th International Conference on Ceramic Processing. doi:10.1016/S0955-2219(03)00222-X.

[37] R. K. Bordia, S.-J. L. Kang, E. A. Olevsky, Current understanding and future research directions at the onset of the next century of sintering science and technology, Journal of the American Ceramic Society 100 (6) (2017) 2314–2352. doi:10.1111/jace.14919.

[38] D. Bouvard, S. Charmond, C. Carry, Finite element modelling of microwave sintering, Ceramic Transactions 209 (2010) 173–180.

[39] R. Bordia, G. Scherer, On constrained sintering—i. constitutive model for a sintering body, Acta Metallurgica 36 (9) (1988) 2393–2397. doi:10.1016/0001-6160(88)90189-7.

[40] C. Maruccio, P. Bene, A. Gerardi, D. Bardaro, Integration of cad, cae and cam procedures for ceramic components undergoing sintering, Journal of the European Ceramic Society 36 (9) (2016) 2263–2275, cERMODEL 2015 Modelling and simulation meet innovation in Ceramics Technology. doi:10.1016/j.jeurceramsoc.2016.01.001.

[41] A. Safonov, S. Chugunov, A. Tikhonov, M. Gusev, I. Akhatov, Numerical simulation of sintering for 3d-printed ceramics via sovs model, Ceramics International 45 (15) (2019) 19027–19035. doi:10.1016/j.ceramint.2019.06.144.

[42] COMSOL Multiphysics v6.2, COMSOL AB, Stockholm, Sweden (2020). URL www.comsol.com

[43] K. W. Schlichting, N. P. Padture, P. G. Klemens, Thermal conductivity of dense and porous yttria-stabilized zirconia, Journal of Materials Science 36 (12) (2001) 3003–3010. doi:10.1023/A:1017970924312.

[44] S. Badwal, Zirconia-based solid electrolytes: microstructure, stability and ionic conductivity, Solid State Ionics 52 (1) (1992) 23–32. doi:10.1016/0167-2738(92)90088-7.

[45] J. Janek, C. Korte, Electrochemical blackening of yttria-stabilized zirconia – morphological instability of the moving reaction front, Solid State Ionics 116 (3) (1999) 181–195. doi:10.1016/S0167-2738(98)00415-9.

[46] Y. Dong, H. Wang, I.-W. Chen, Electrical and hydrogen reduction enhances kinetics in doped zirconia and ceria: I. grain growth study, Journal of the American Ceramic Society 100 (3) (2017) 876–886. doi:10.1111/jace.14615.

[47] M. Mazaheri, A. Simchi, M. Dourandish, F. Golestani-Fard, Master sintering curves of a nanoscale 3Y-TZP powder compacts, Ceramics International 35 (2) (2009) 547–554. doi: 10.1016/j.ceramint.2008.01.008.

[48] Y.-S. Kwon, Y. Wu, P. Suri, R. M. German, Simulation of the sintering densification and shrinkage behavior of powder-injection-molded 17-4 PH stainless steel, Metallurgical and Materials Transactions A 35 (1) (2004) 257–263. doi:10.1007/s11661-004-0126-4.

Table 1. Gauge sections in mm of the four samples

Sample	width × thickness × length (hole-to-hole)
OB	5.84 × 2.66 × 23
TB	5.80 × 2.70 × 24
OD	5.85 × 3.34 × 22
TD	5.92 × 4.04 × 23

Table 2. Values chosen for k_h, with h = 1,⋯ ,5.

k_1 [−]	k_2 [−]	k_3 [−]	k_4 [$s^{-1}\cdot K^{-1}$]	k_5 [J/mol]
0	2	-1	1.25×10^{15}	290×10^{3}

Table 3. Values of the green body and fully sintered material properties used in the numerical models.

State of sample	ρ [kg/m^3]	σ [S/m]	Q [J/mol]	k [W/mK]
Green body	3025	677×10^{3}	139×10^{3}	0.4
Fully sintered	6050	37×10^{3}	96×10^{3}	2.5

Table 4. Steady-state temperature, density, open porosity, mean grain size and flexural strength of the four FSed 3YSZ samples. Steady state temperature is evaluated from Eq. (1) and other results are derived from experiments.

Sample	Steady-state temperature [K]	Relative density [%]	Open porosity [%]	Mean grain size (core) [μm]	Mean grain size (surface) [μm]	Flexural strength [MPa]
OB	1598	92.7	4.2	167	80	1203 ± 17
TB	1643	96.0	1.9	148	92	1336 ± 19
OD	1628	95.5	2.4	157	83	1258 ± 16
TD	1658	99.7	0.2	137	111	1501 ± 15

Table 5. Temperatures predicted by the numerical model both overall and at the steady state compared against the sample mean temperature derived from experimental data ($T^{s}_{\mathrm{mean-exp}}$), using the black-body radiation model Eq. (1). Results are in *K*.

−	OB	TB	OD	TD
T^{s}_{mean} (Steady state)	1554	1568	1579	1596
T^{v}_{max} (Steady state)	1645	1650	1658	1680
T^{v}_{mean} (Steady state)	1585	1608	1615	1637
$T^{v}_{\mathrm{max-t}}$ (Overall)	1696	1657	1670	1681
$T^{v}_{\mathrm{max-t}} - T^{v}_{\mathrm{mean}}$	111	49	55	44
$T^{s}_{\mathrm{mean-exp}}$ (Steady state)	1600	1642	1644	1658

Table 6. Comparison of experimentally measured and numerically predicted relative density of the four specimens.

−	OB	TB	OD	TD
Experimental	92.7%	96.0%	95.5%	99.7%
Numerical	93.5%	95.6%	95.1%	97.7%
Error	0.8%	0.4%	0.5%	1.9%

Table 7. Fraction of the gauge volume with relative density higher than 95% for the four numerical models. The gauge volume was defined as the part of the sample between the drilled holes at the ends.

−	OB	TB	OD	TD
Volume Fraction	40%	65%	60%	85%

Figure 1

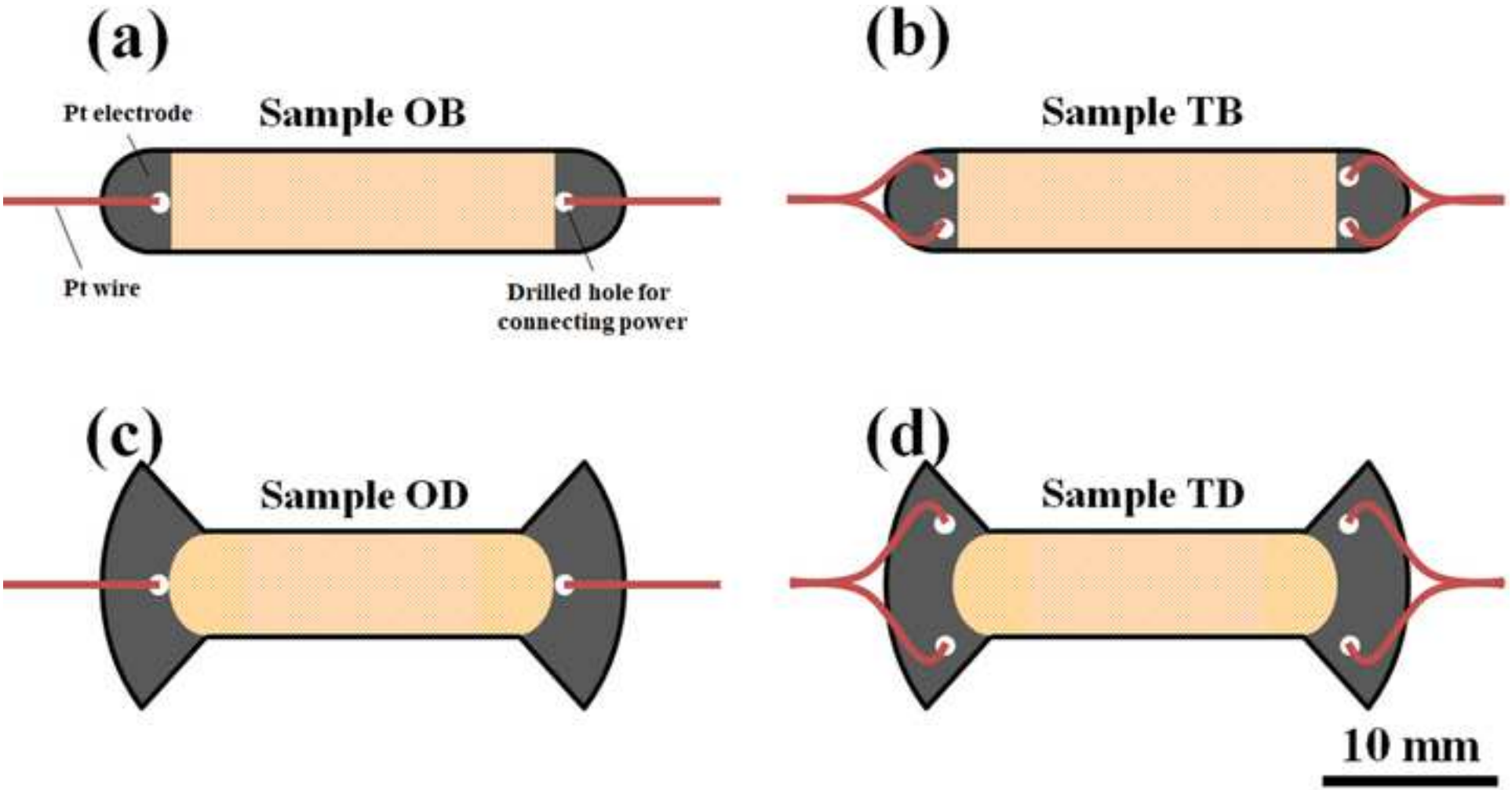

Figure 2

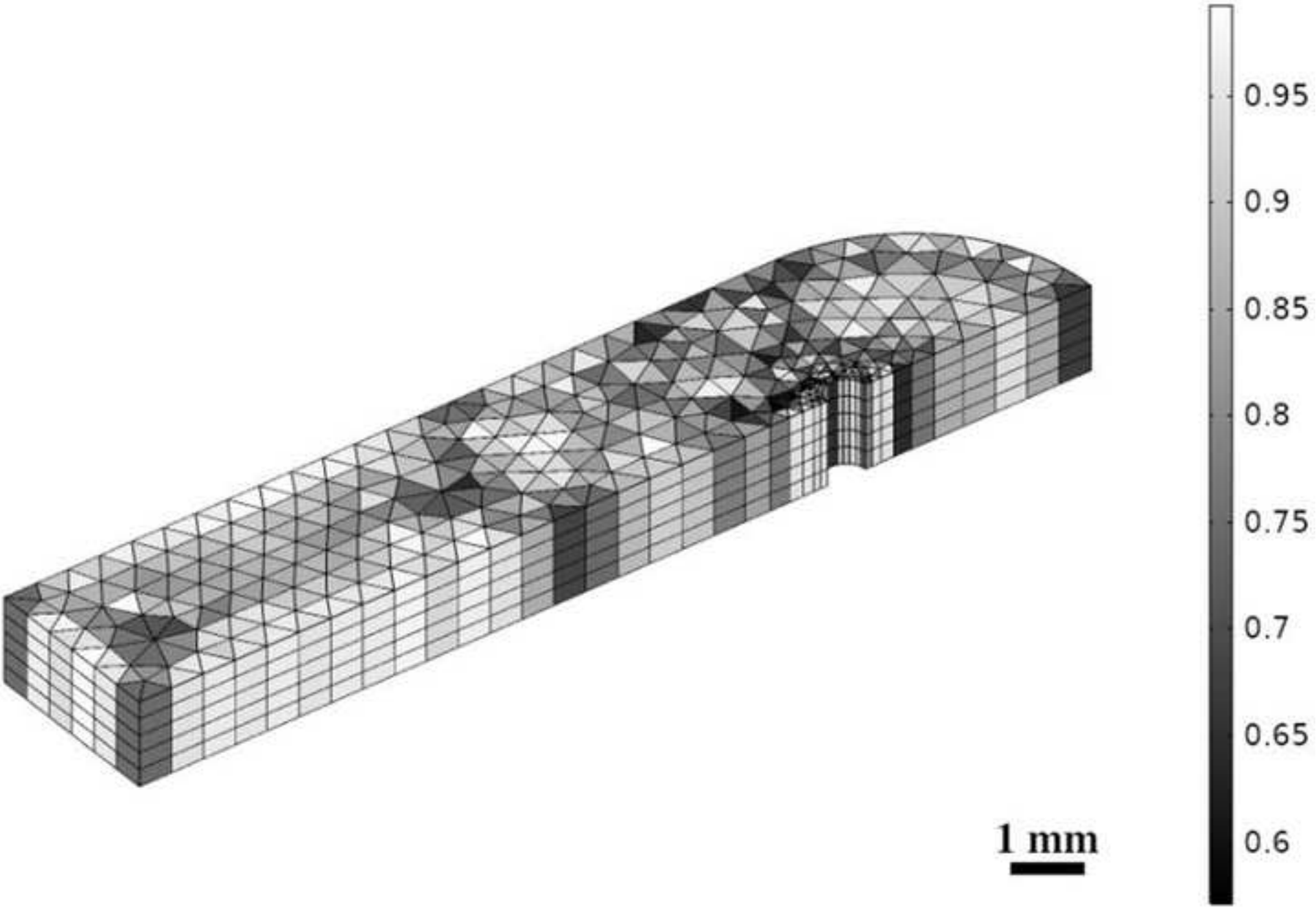

Figure 3

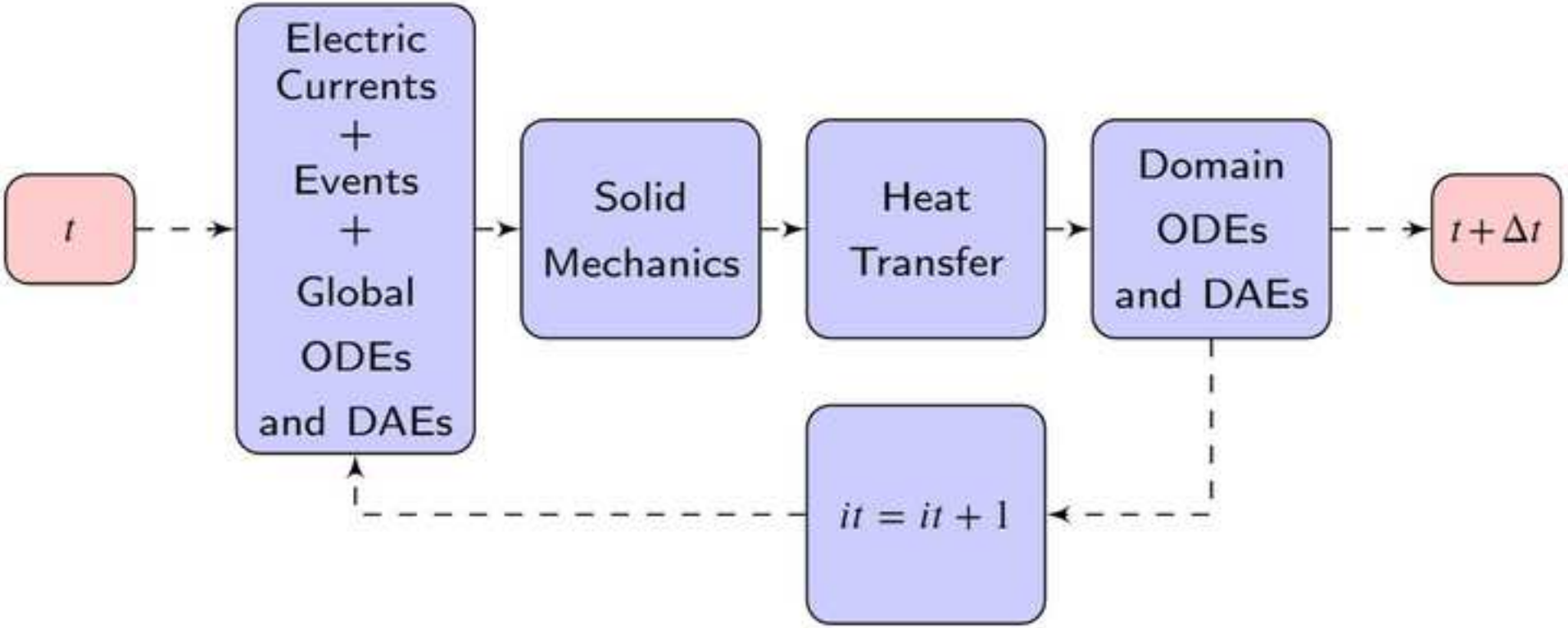

Figure 4a

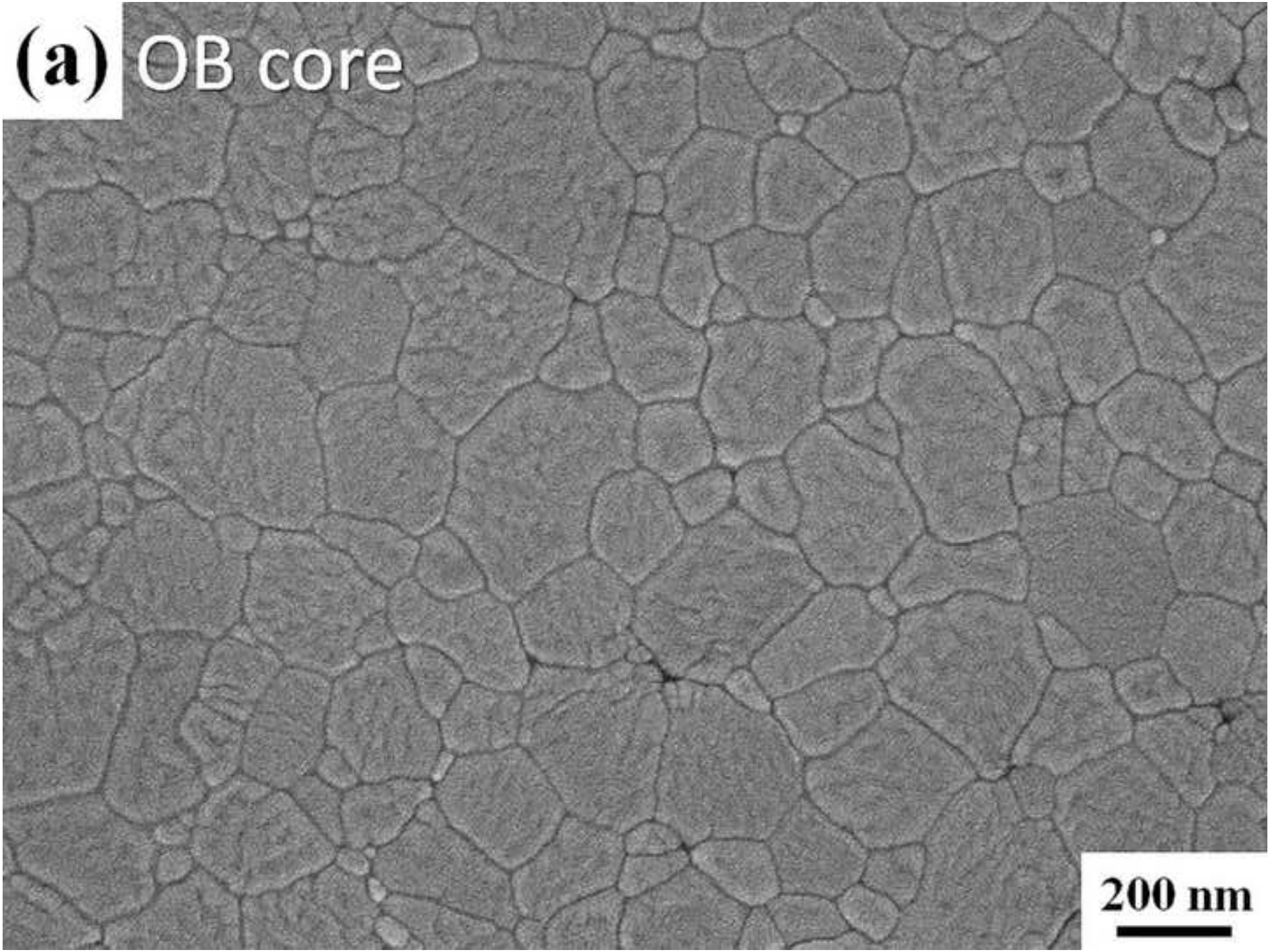

Figure 4b

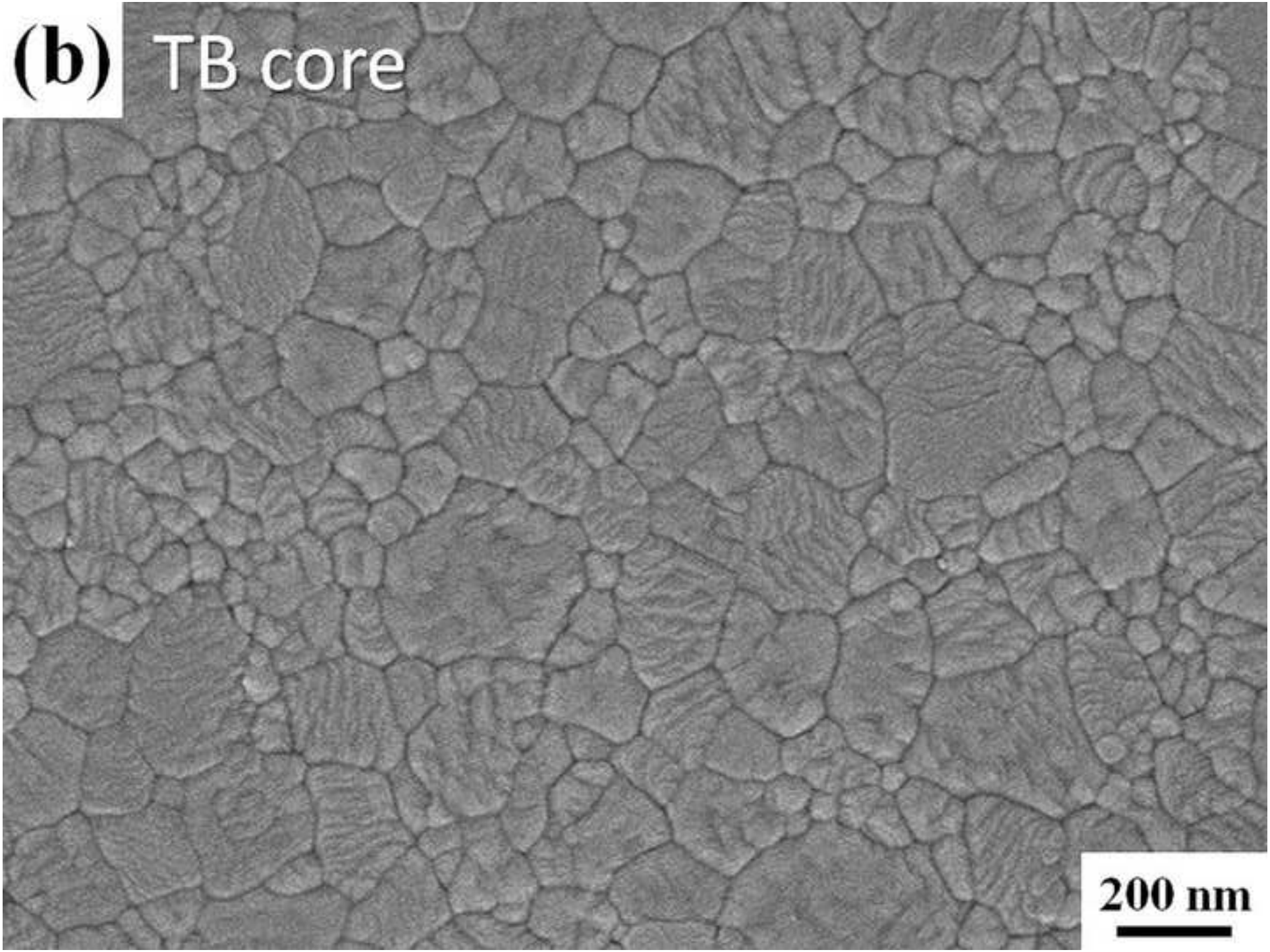

Figure 4c

Click here to access/download;Figure;Figure 4c.jpg

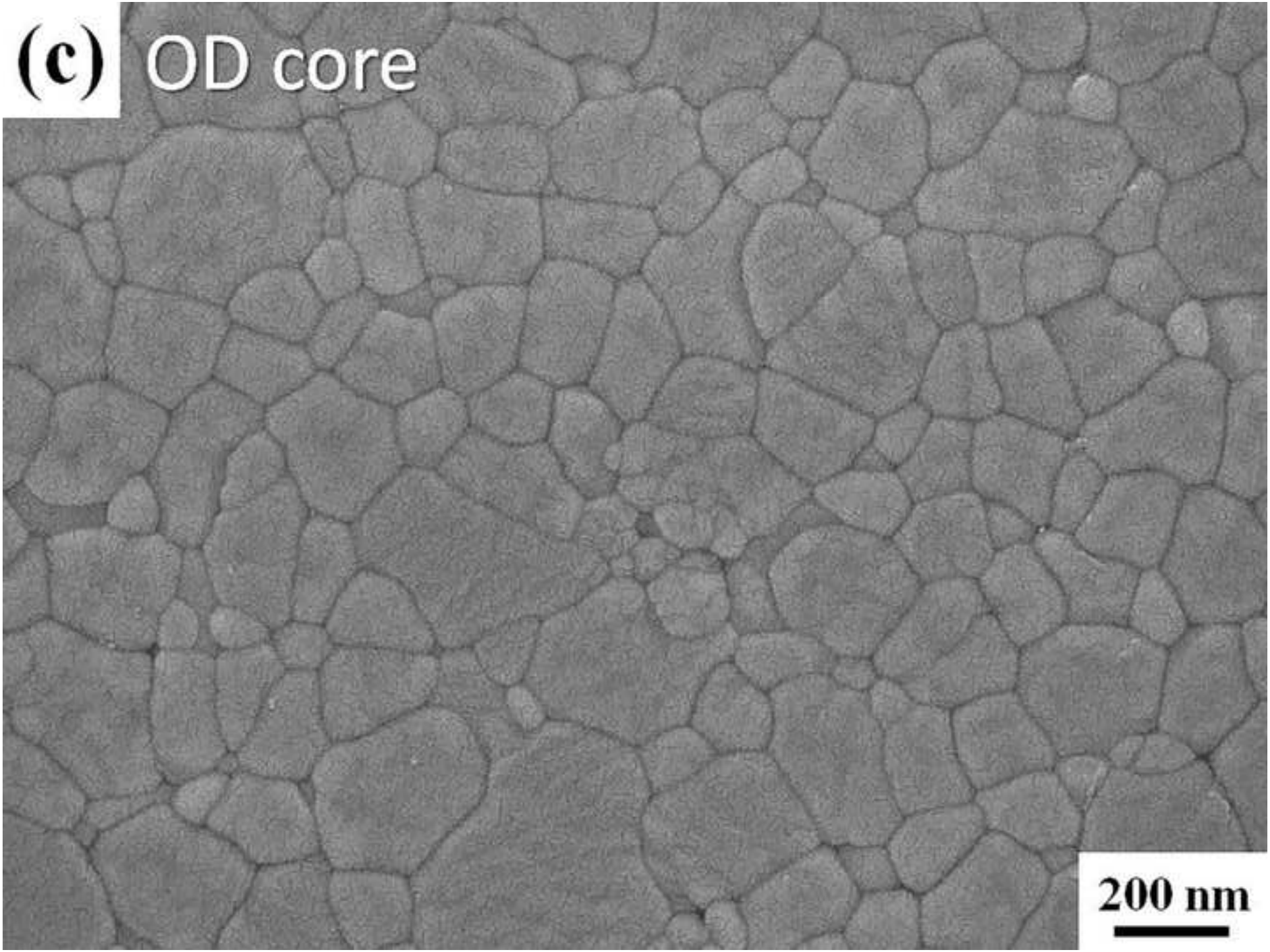

Figure 4d

Click here to access/download;Figure;Figure 4d.jpg

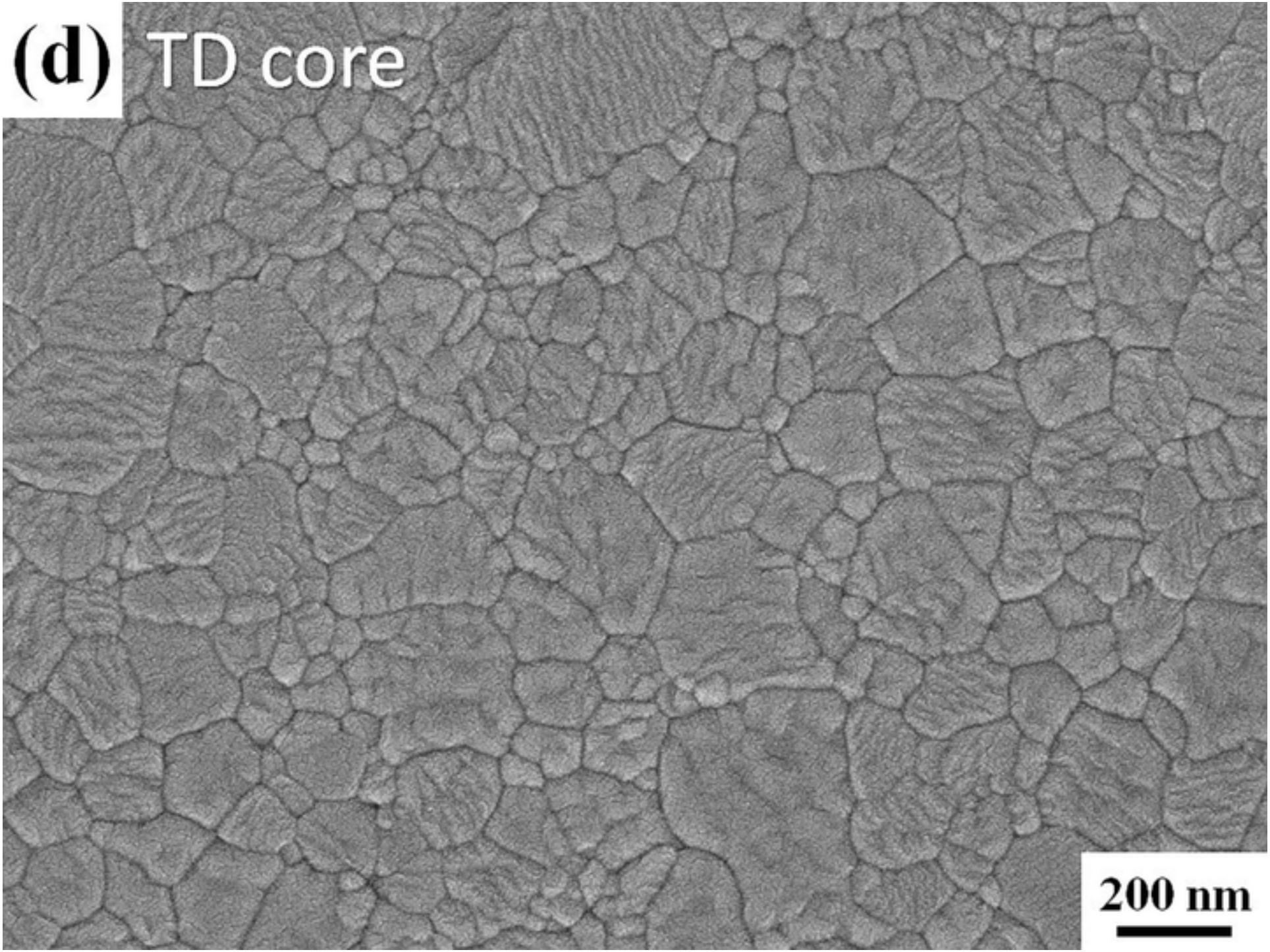

Figure 4e

Click here to access/download;Figure;Figure 4e.jpg

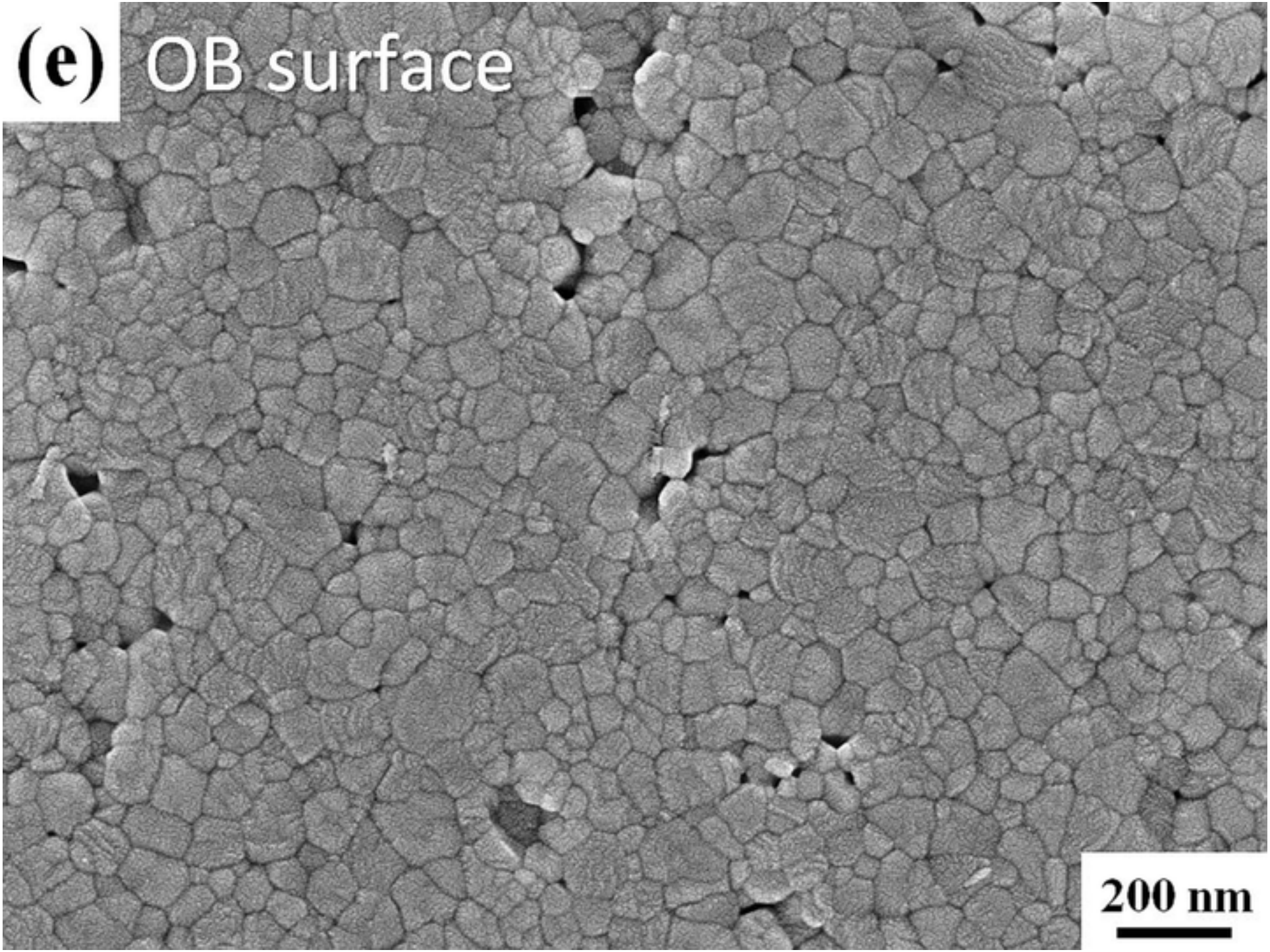

Figure 4f

Click here to access/download;Figure;Figure 4f.jpg

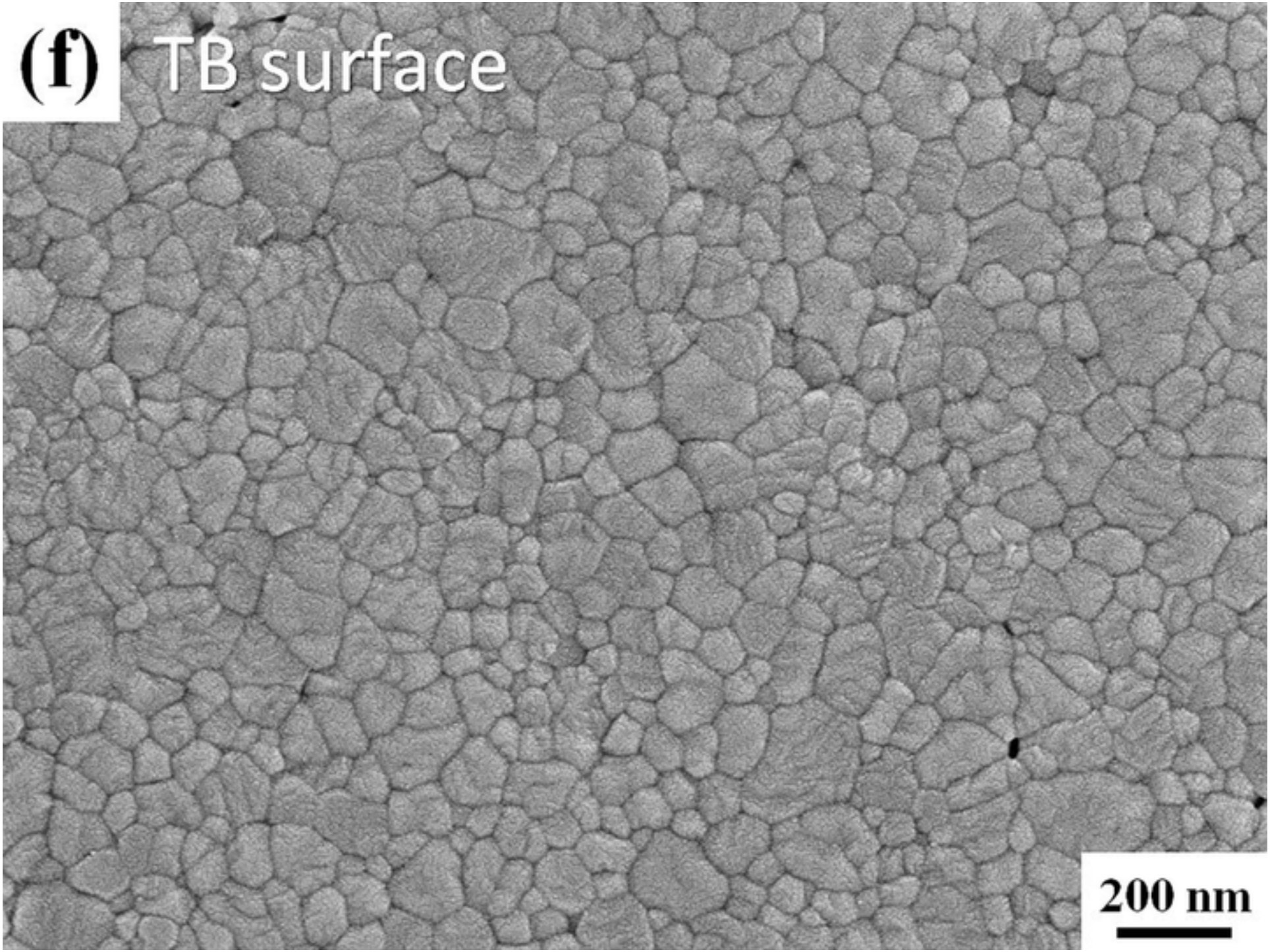

Figure 4g

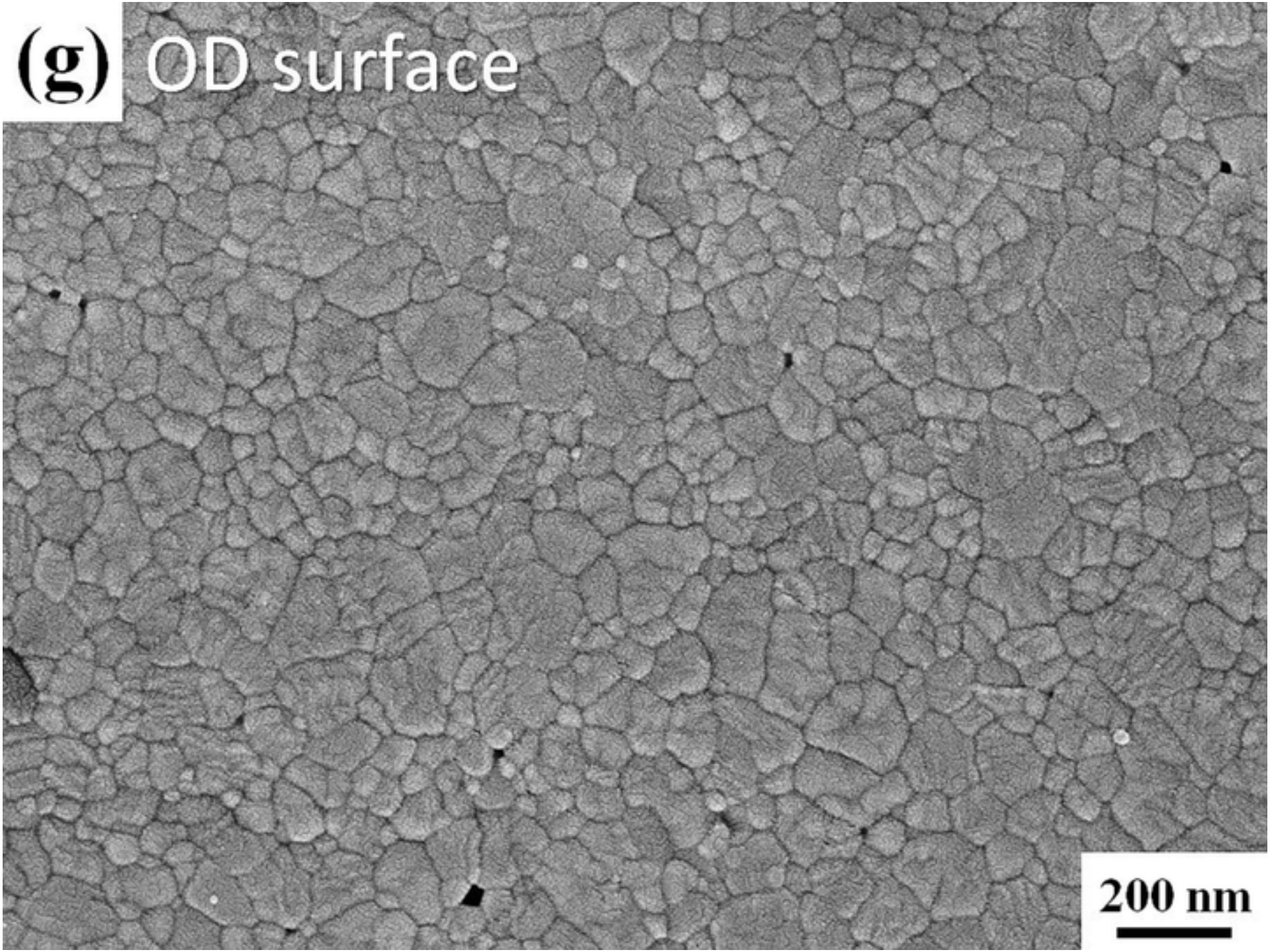

Figure 4h

Click here to access/download;Figure;Figure 4h.jpg

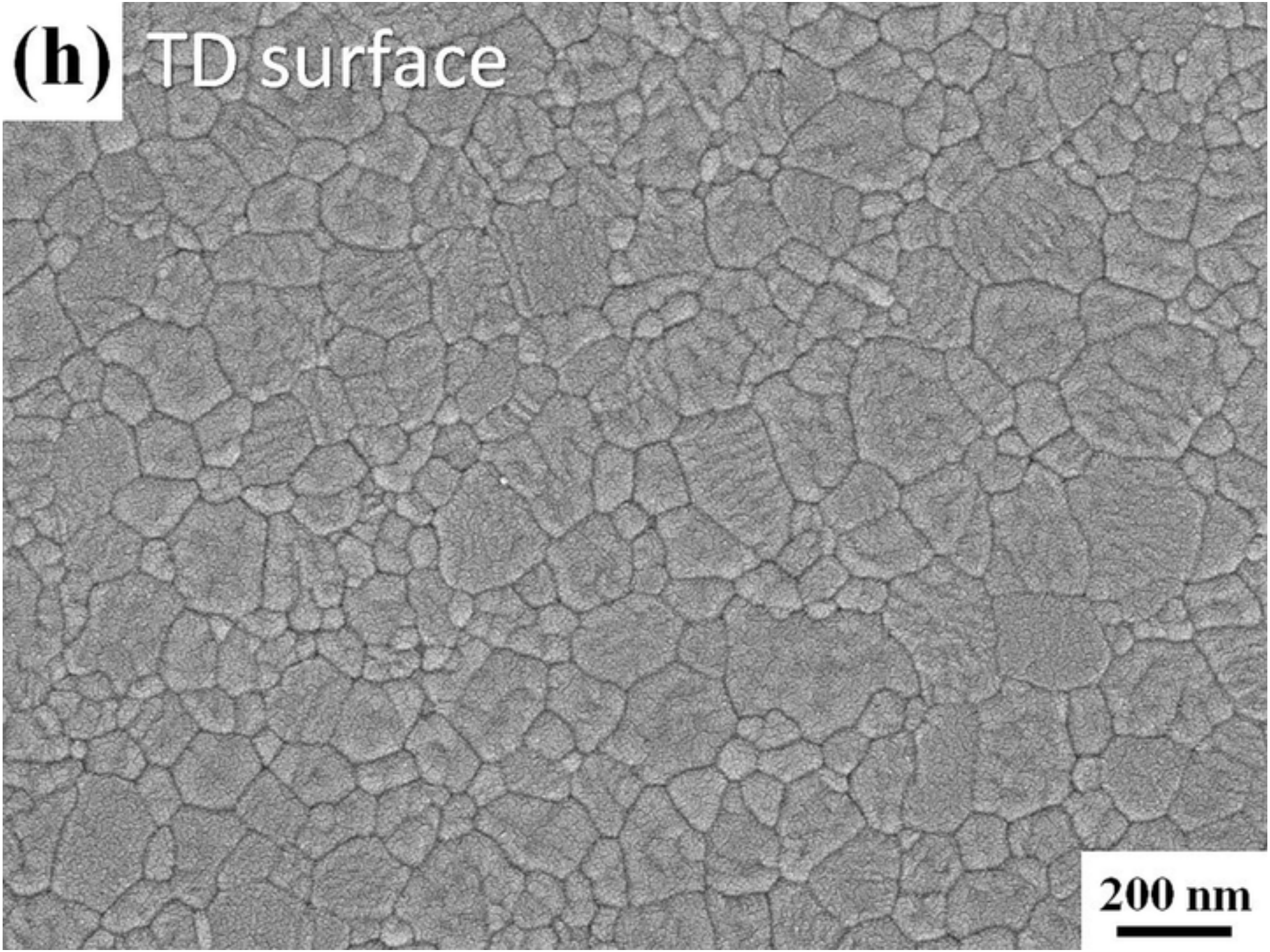

Figure 5a

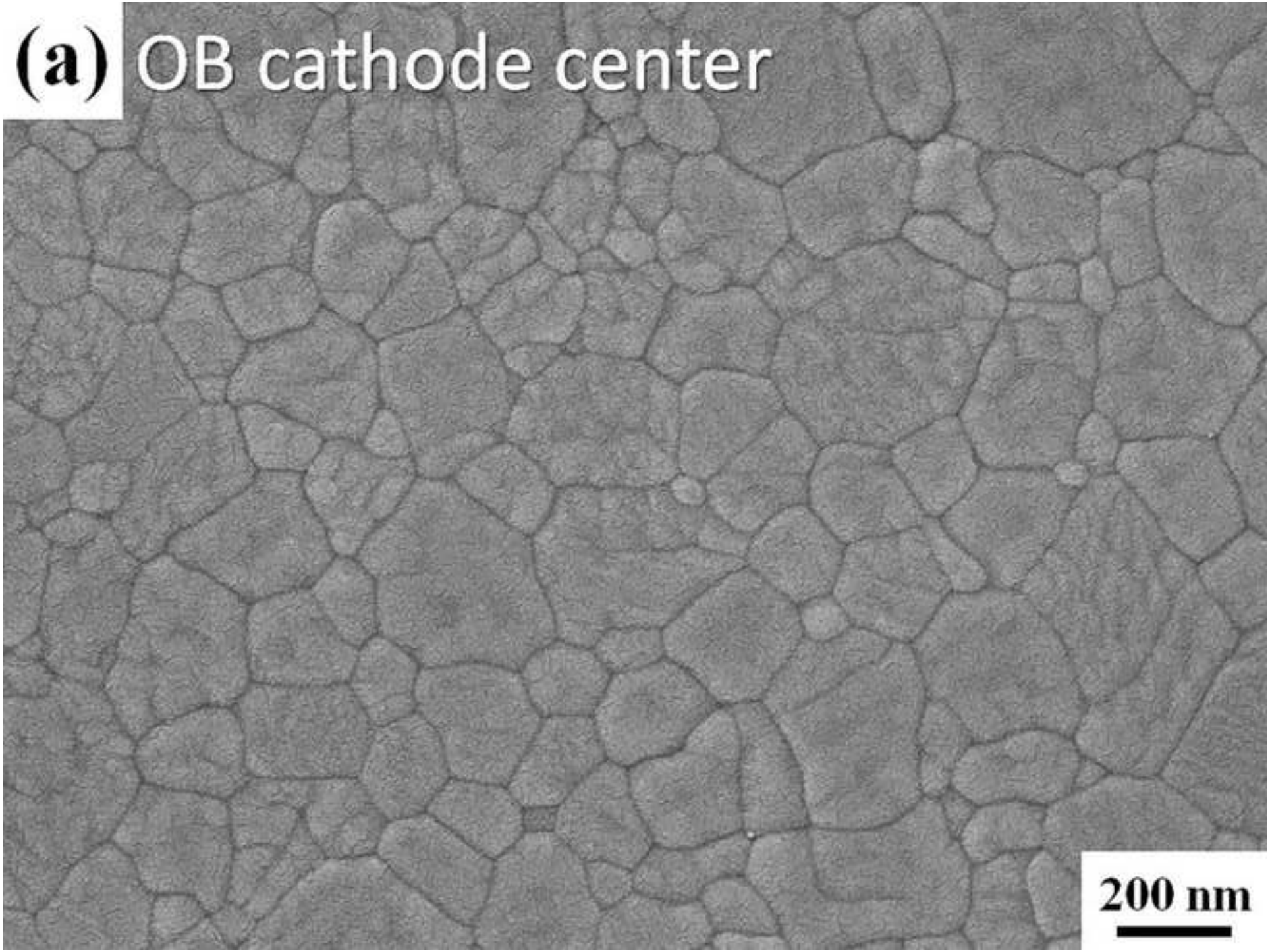

Figure 5b

Click here to access/download;Figure;Figure 5b.jpg

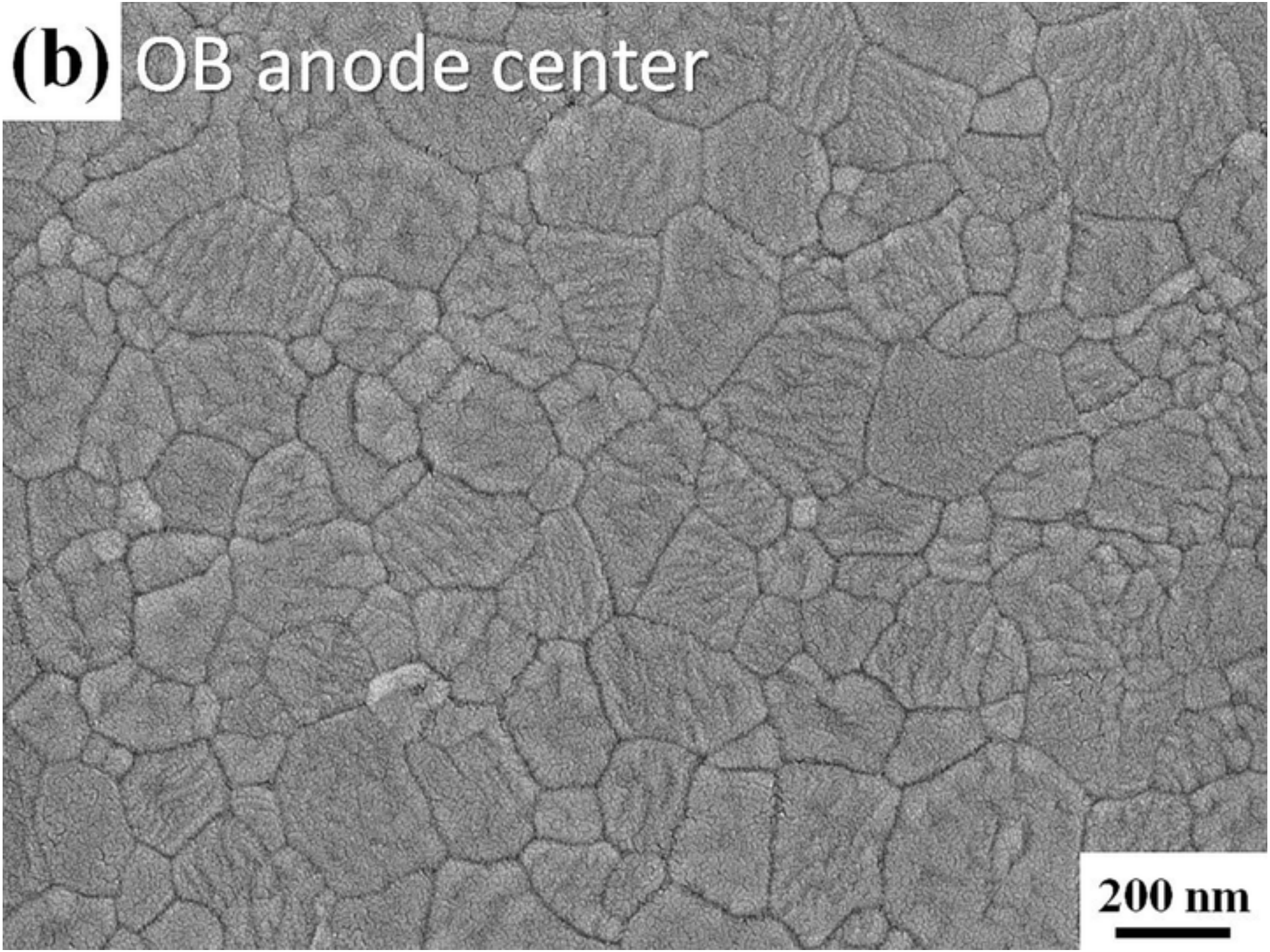

Figure 6

Click here to access/download;Figure;Figure 6.jpg

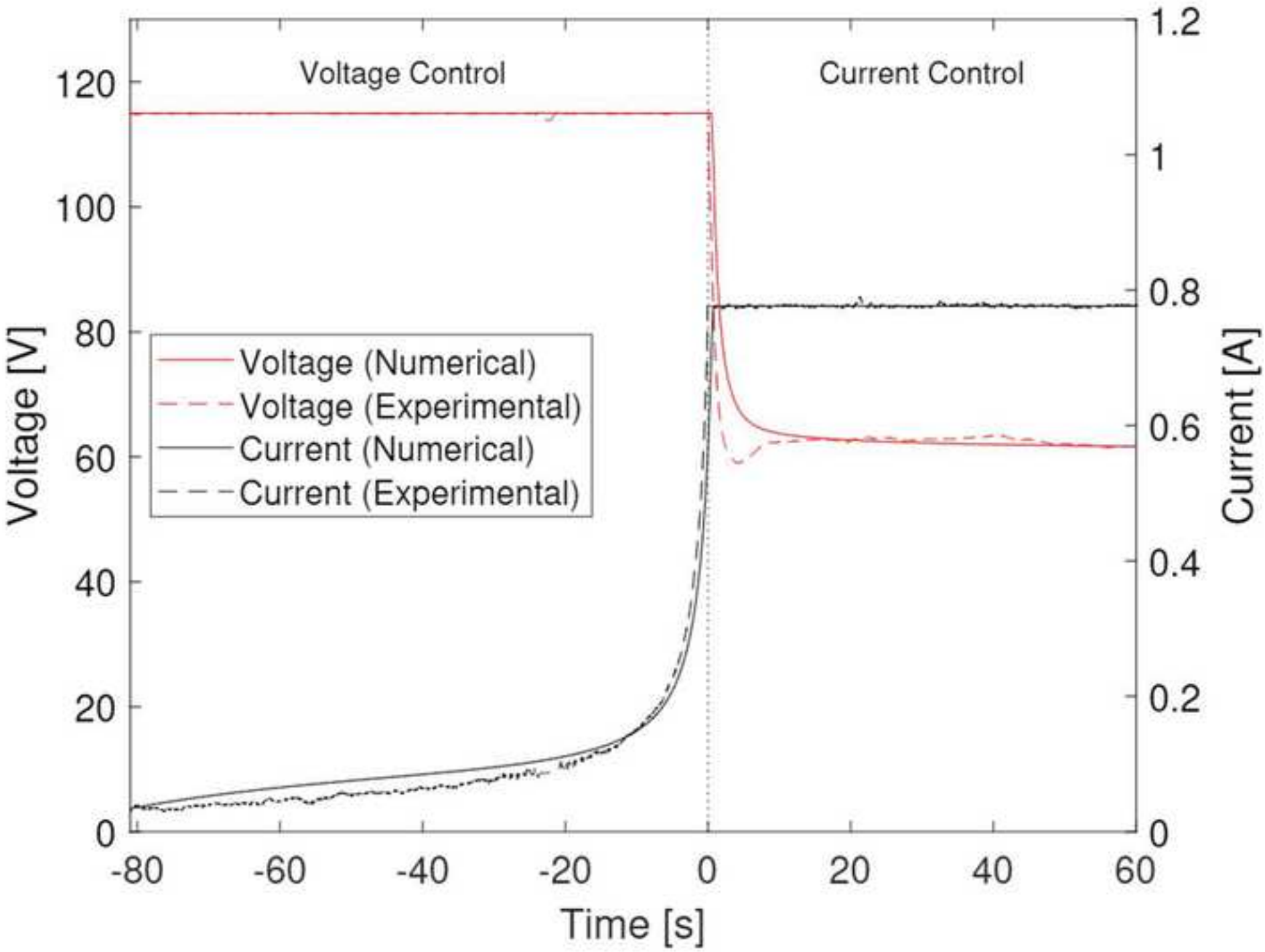

Figure 7

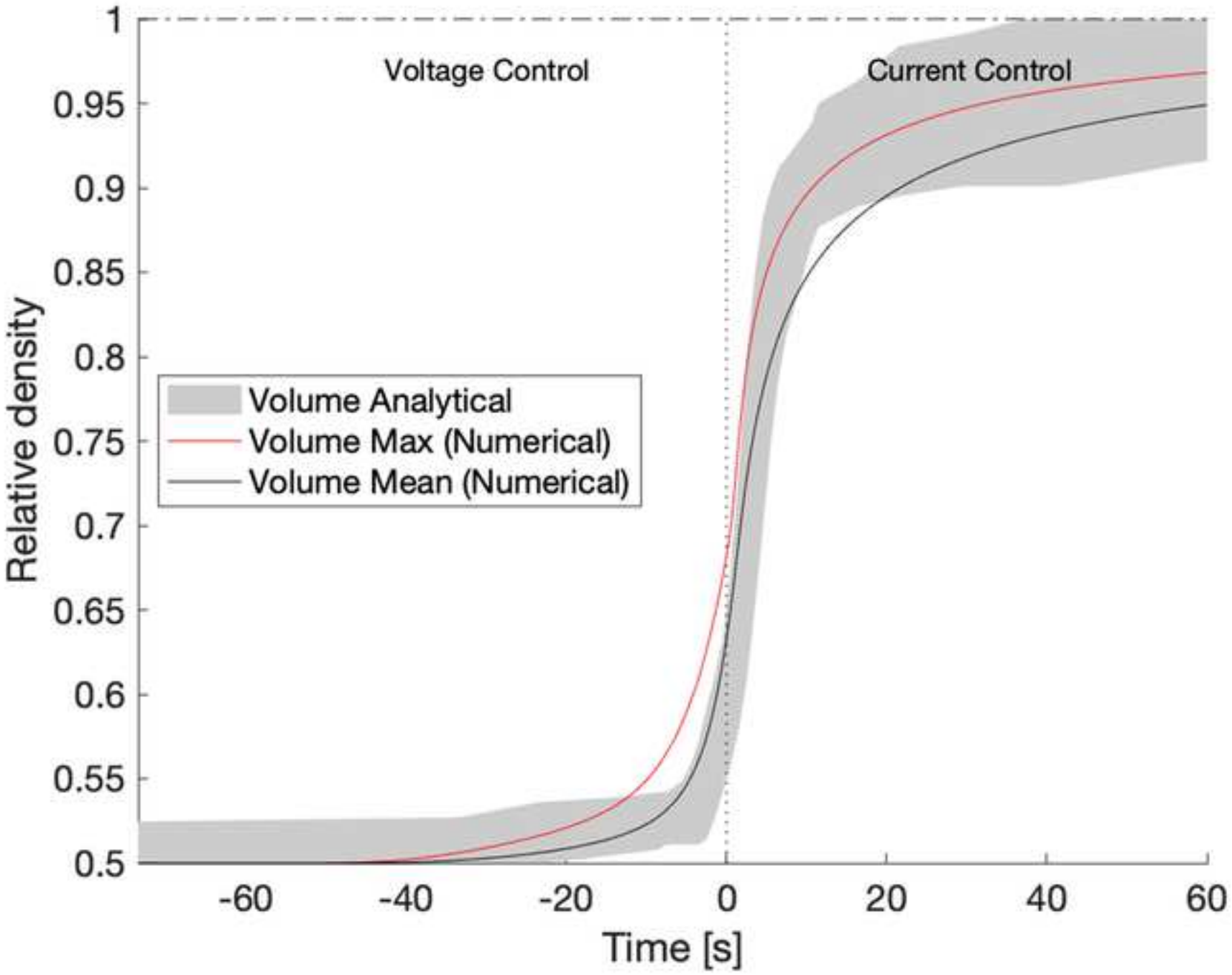

Figure 8a

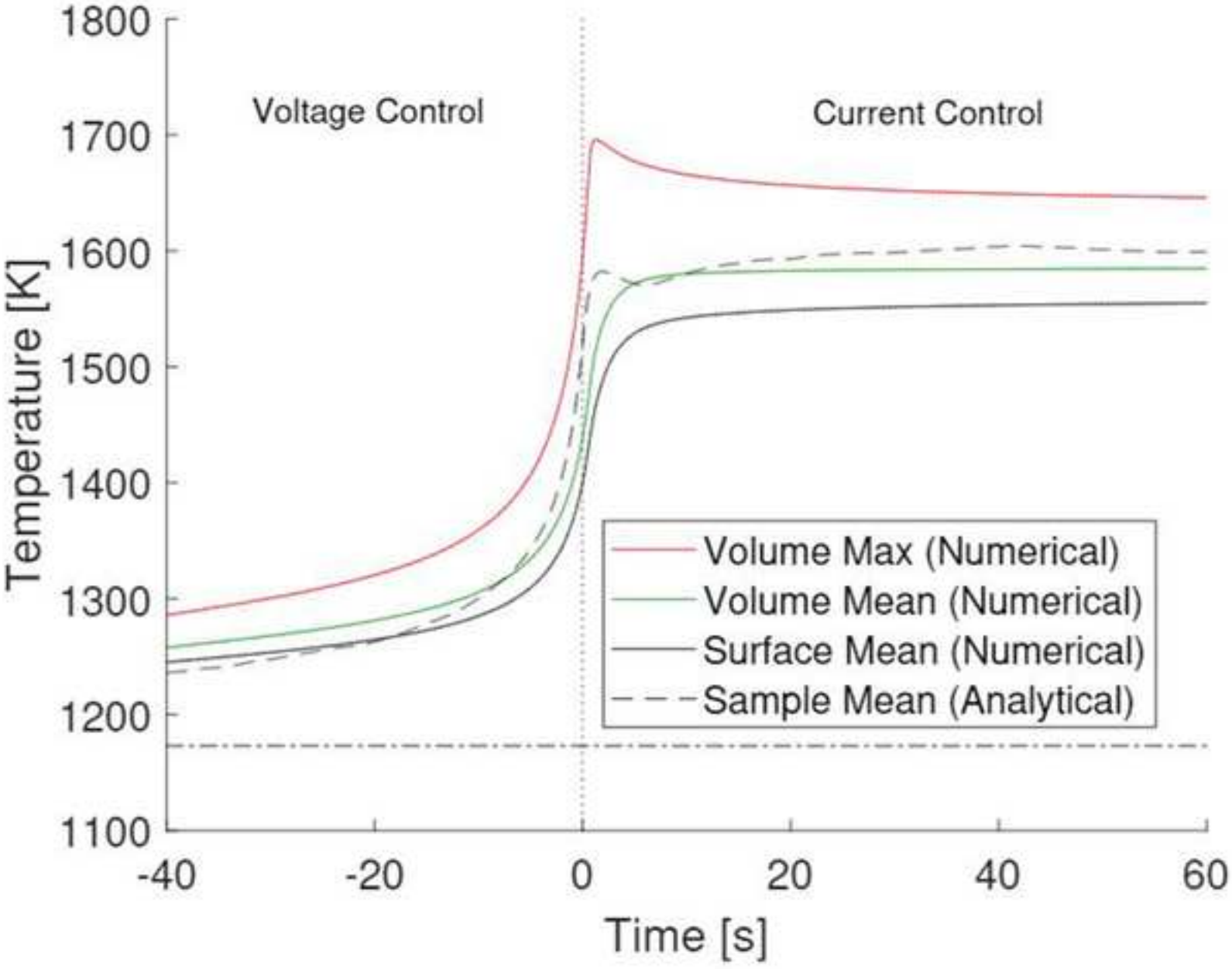

(a) OB temperature profile

Figure 8b

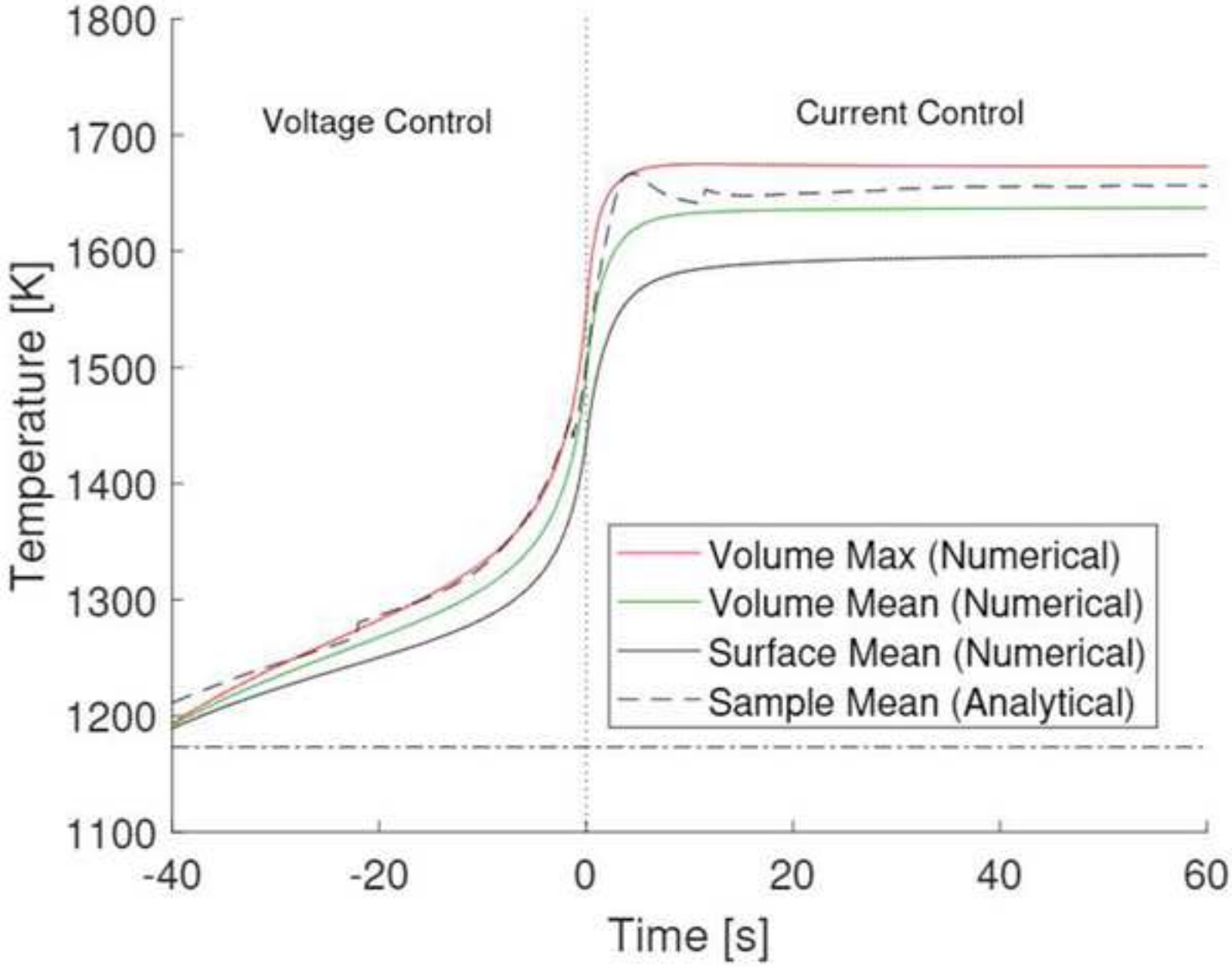

(b) TD temperature profile

Figure 9

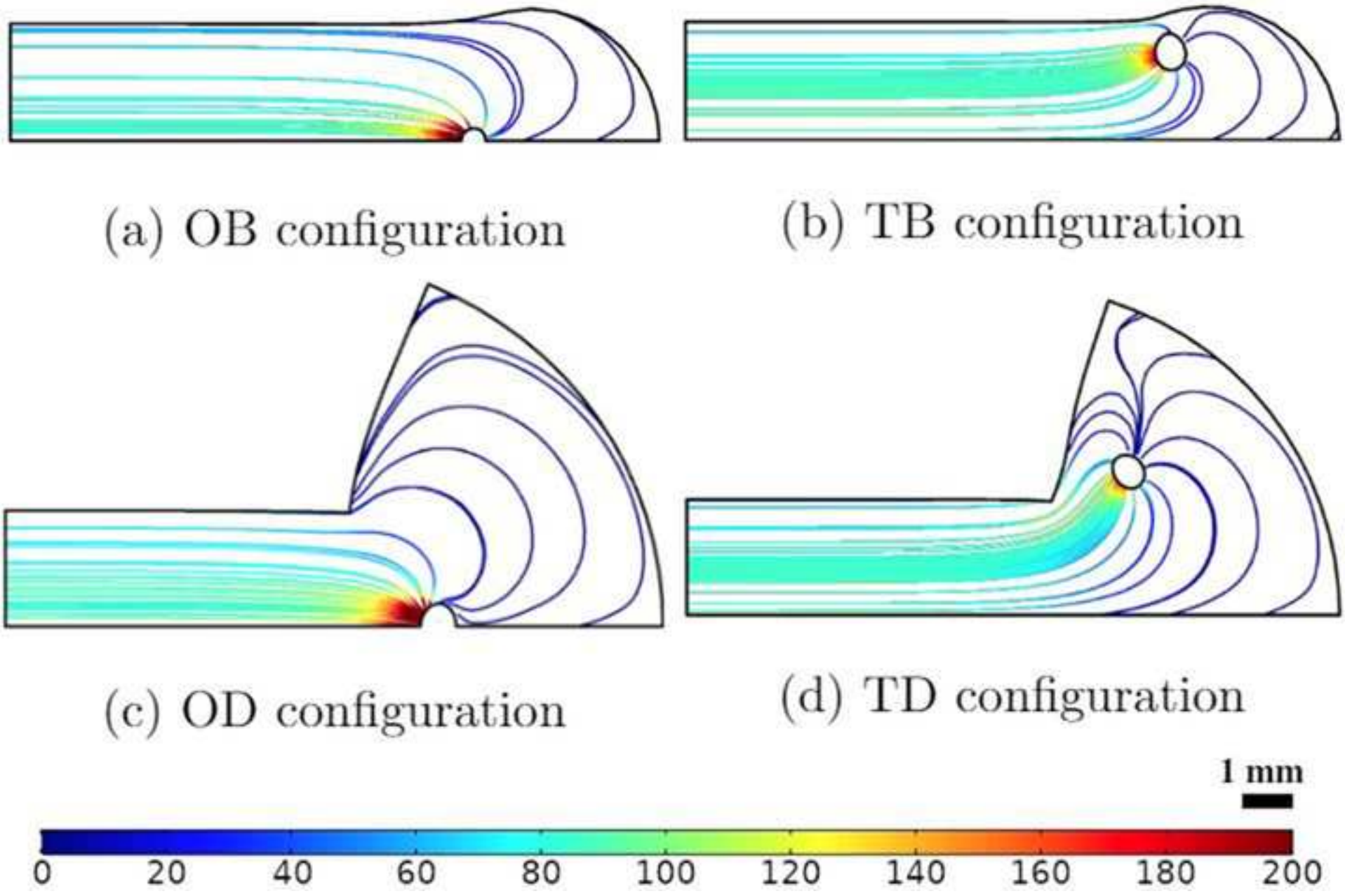

Figure 10

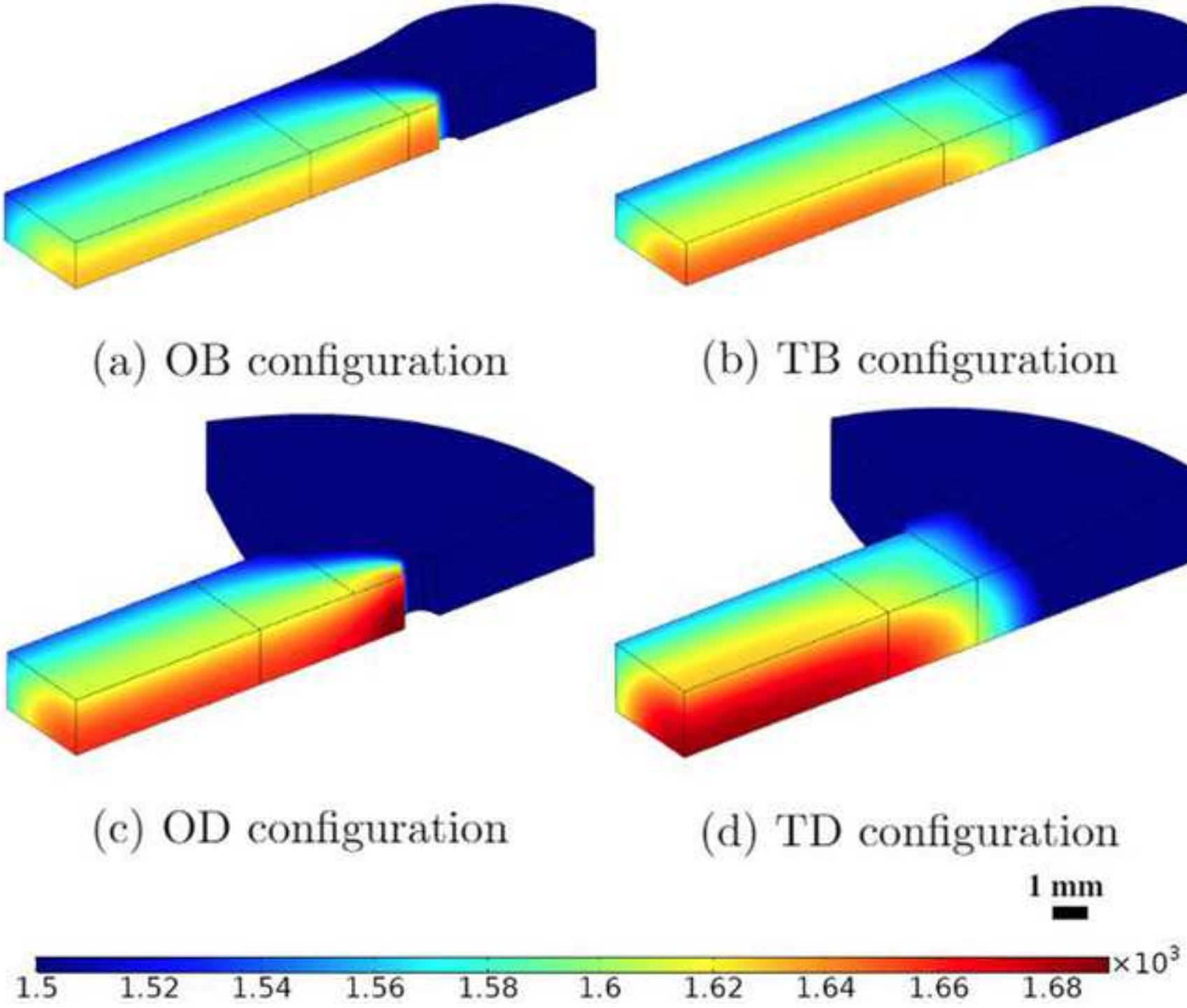

Figure 11

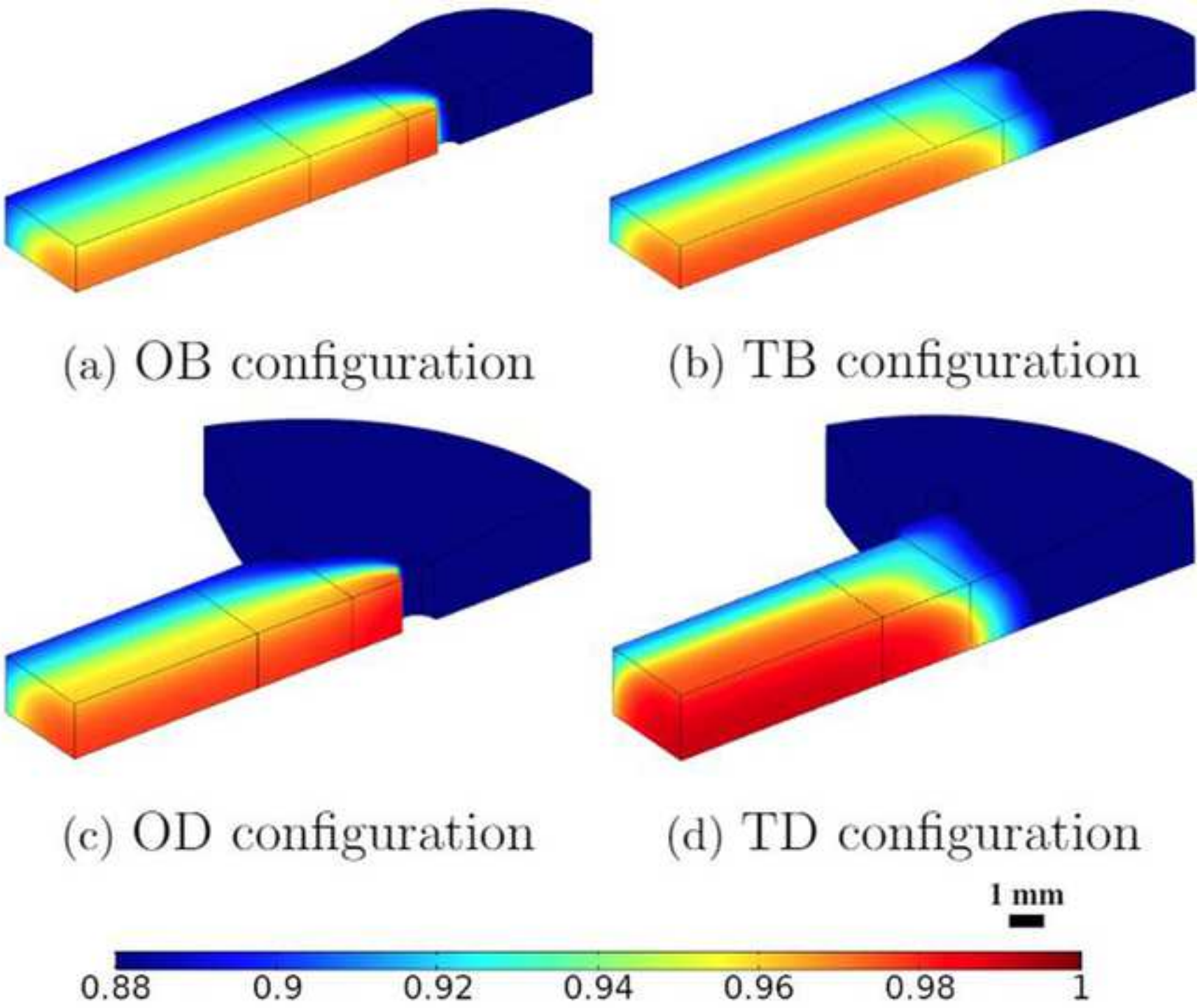

Figure 12

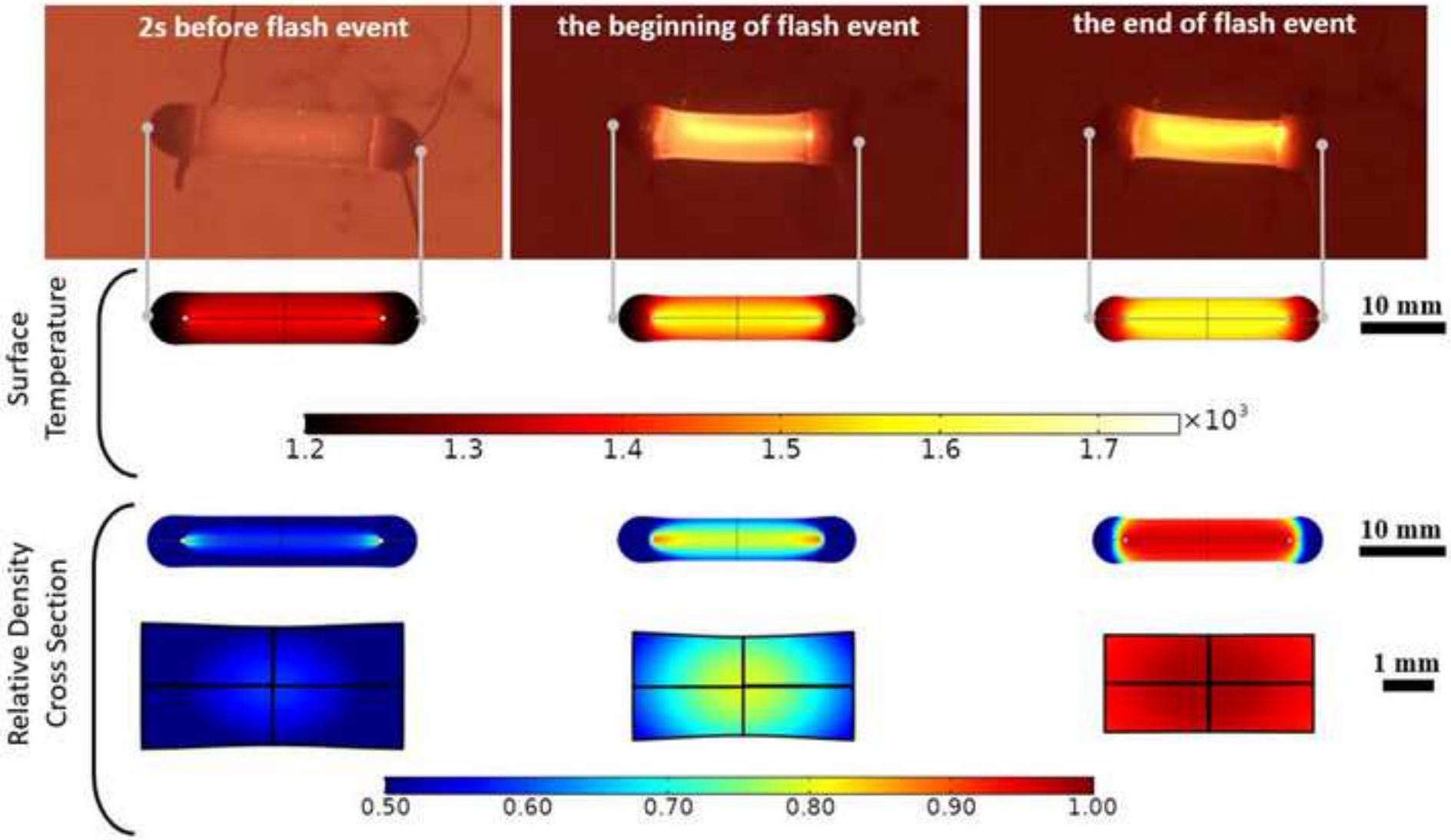

Figure 13

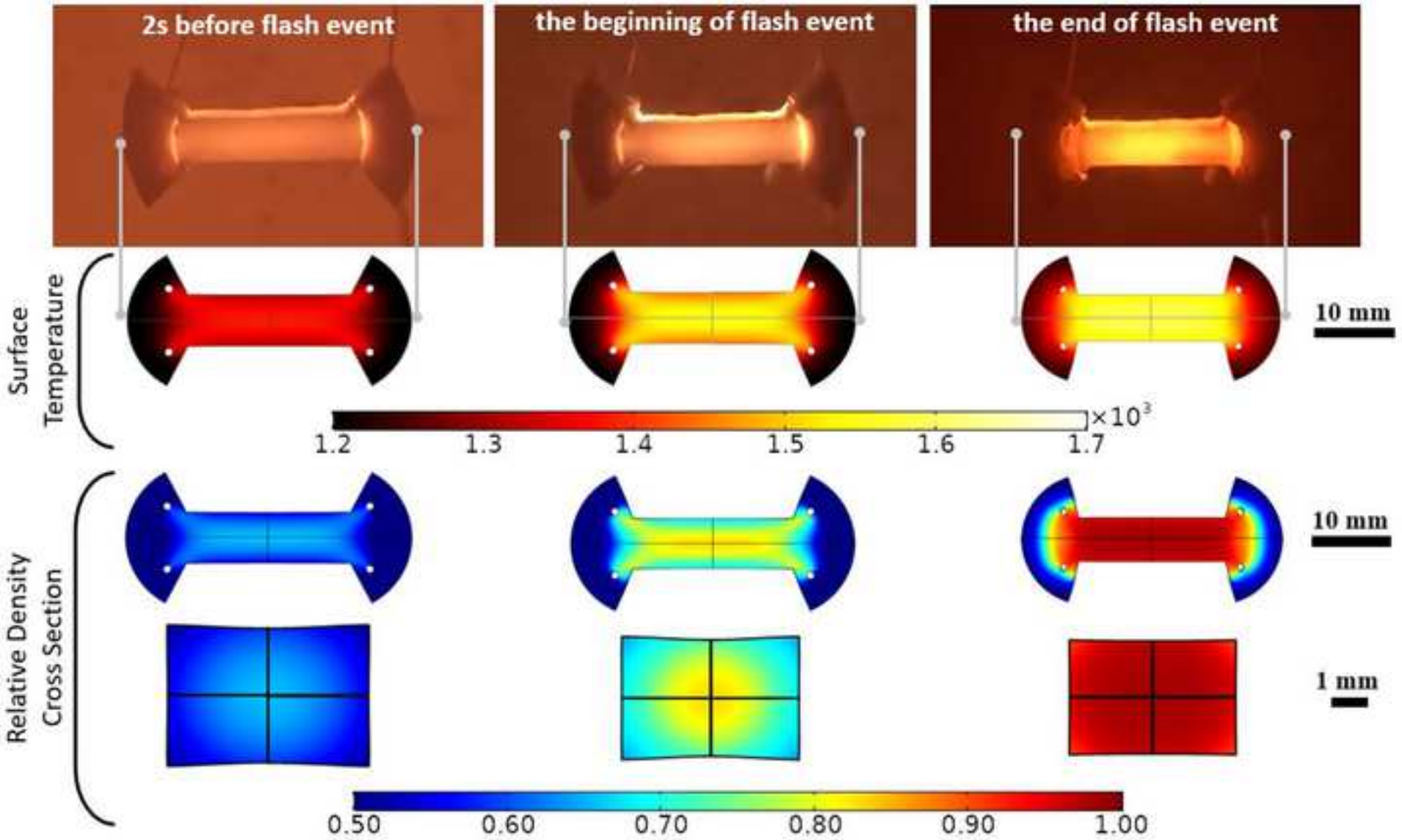

Figure Captions

Figure 1. Schematics of the four 3YSZ samples for flash sintering experiments: (a) Sample OB with bar-shape and one drilled hole at each end, (b) Sample TB with bar-shape and two drilled holes at each end, (c) Sample OD with dogbone-shape and one drilled hole at each end, (d) Sample TD with dogbone-shape and two drilled holes at each end. The grey regions represent the Pt paste and the drilled holes are connected to the power supply through Pt wire.

Figure 2. Model of Sample OB with symmetries and the grey-scale bar showing the mesh quality.

Figure 3. Segregated solver scheme: the physical processes are solved in four internal steps, which are repeated until the global tolerance is under 10^{-6}. The time step Δt is adaptively chosen by the solver.

Figure 4. SEM images of the polished and thermally etched cross-sections from core (top row) and surface (bottom row) of 3YSZ samples: (a, e) Sample OB, (b, f) Sample TB, (c, g) Sample OD, (d, h) Sample TD.

Figure 5. SEM images of the polished and thermally etched cross-section centers from (a) cathode and (b) anode of Sample OB after flash sintering.

Figure 6. Validation of difference of potential (red) and current (black) numerical predictions (solid line) against experimental results (dashed line) during the FS of Sample OB. The critical instant for the transition of voltage control to current control stage was defined as t = 0 s.

Figure 7. Comparison of the density evaluated from experimental estimation (grey area) against numerical prediction of the average (black) and maximum (red) density for the OB specimen.

Figure 8. Comparison of the sample mean temperature evaluated from experimental data by using the black-body radiation model (Eq. (1)) against the numerical prediction of temperatures (surface mean, volume mean, and volume maximal) for the OB and TD specimens.

Figure 9. Current density streamlines (mA/mm^2) in four YSZ samples at the end of FS analysed by the numerical model.

Figure 10. Temperature distribution (in K) in four YSZ samples at the end of FS analysed by the numerical model.

Figure 11. Relative density distribution in four YSZ samples at the end of FS analysed by the numerical model.

Figure 12. Snapshots of the OB specimen at 2s before, at the beginning and at the end of flash event, alongside the corresponding numerical predictions of surface temperature and relative density.

Figure 13. Snapshots of the TD specimen at 2s before, at the beginning and at the end of flash event, alongside the corresponding numerical predictions of surface temperature and relative density.

Table Captions

Table 1. Gauge sections in mm of the four samples.

Table 2. Values chosen for k_h, with h = 1,⋯ ,5.

Table 3. Values of the green body and fully sintered material properties used in the numerical models.

Table 4. Steady-state temperature, density, open porosity, mean grain size and flexural strength of the four FSed 3YSZ samples. Steady state temperature is evaluated from Eq. (1) and other results are derived from experiments.

Table 5. Temperatures predicted by the numerical model both overall and at the steady state compared against the sample mean temperature derived from experimental data ($T^{S}_{\mathrm{mean-exp}}$), using the black-body radiation model Eq. (1). Results are in *K*.

Table 6. Comparison of experimentally measured and numerically predicted relative density of the four specimens.

Table 7. Fraction of the gauge volume with relative density higher than 95% for the four numerical models. The gauge volume was defined as the part of the sample between the drilled holes at the ends.